University of South Florida
Scholar Commons

Graduate Theses and Dissertations   Graduate School

2010

Fluorescence molecular tomography: A new volume reconstruction method

Stephen Joseph Shamp
University of South Florida

Follow this and additional works at: http://scholarcommons.usf.edu/etd

Part of the American Studies Commons

Fluorescence Molecular Tomography: A New Volume Reconstruction Method

by

Stephen Joseph Shamp

A thesis submitted in partial fulfillment
of the requirements for the degree of
Master of Science in Electrical Engineering
Department of Electrical Engineering
College of Engineering
University of South Florida

Major Professor: Vijay K. Jain, Ph.D.
Andrew Hoff, Ph.D.
Gokhan Mumcu Ph.D.

Date of Approval:
July 6, 2010

Keywords: fmt, khatri-rao, diffuse optical tomography, singular value decomposition,
high spatial sampling, overdetermined

Acknowledgements

I wish to express my gratitude to my major professor, Dr. Vijay K. Jain for his guidance

and inspiration throughout this research and my graduate studies.

I also thank my committee members Dr. Andrew Hoff and Dr. Gokhan Mumcu for their

helpful comments and suggestions.

Finally, I would like to thank my wife, parents, and family for their love and

encouragement.

Table of Contents

List of Tables

List of Figures

iv

Fluorescence Molecular Tomography: A New Volume Reconstruction Method

Stephen Joseph Shamp

Abstract

Medical imaging is critical for the detection and diagnosis of disease, guided biopsies, assessment of therapies, and administration of treatment. While computerized tomography (CT), magnetic resonance imaging (MRI), positron emission tomography (PET), and ultra-sound (US) are the more familiar modalities, interest in yet other modalities continues to grow. Among the motivations are reduction of cost, avoidance of ionizing radiation, and the search for new information, including biochemical and molecular processes. Fluorescence Molecular Tomography (FMT) is one such emerging technique and, like other techniques, has its advantages and limitations. FMT can reconstruct the distribution of fluorescent molecules *in vivo* using near-infrared radiation or visible band light to illuminate the subject. FMT is very safe since non-ionizing radiation is used, and inexpensive due to the comparatively low cost of the imaging system. This should make it particularly well suited for small animal studies for research. A broad range of cell activity can be identified by FMT, making it a potentially valuable tool for cancer screening, drug discovery and gene therapy.

Since FMT imaging is scattering dominated, reconstruction of volume images is significantly more computationally intensive than for CT. For instance, to reconstruct a

32×32×32 image, a flattened matrix with approximately 10^{10}, or 10 billion, elements must be dealt with in the inverse problem, while requiring more than 100 GB of memory. To reduce the error introduced by noisy measurements, significantly more measurements are needed, leading to a proportionally larger matrix. The computational complexity of reconstructing FMT images, along with inaccuracies in photon propagation models, has heretofore limited the resolution and accuracy of FMT.

To surmount the problems stated above, we decompose the forward problem into a Khatri-Rao product. Inversion of this model is shown to lead to a novel reconstruction method that significantly reduces the computational complexity and memory requirements for overdetermined datasets. Compared to the well known SVD approach, this new reconstruction method decreases computation time by a factor of up to 25, while simultaneously reducing the memory requirement by up to three orders of magnitude. Using this method, we have reconstructed images up to 32×32×32. Also outlined is a two step approach which would enable imaging larger volumes. However, it remains a topic for future research.

In achieving the above, the author studied the physics of FMT, developed an extensive set of original computer programs, performed COMSOL simulations on photon diffusion, and unavoidably, developed visual displays.

1. Introduction

Fluorescence Molecular Tomography (FMT) is a medical imaging technology which uses near-infrared radiation or visible band light to illuminate and reconstruct the distribution of fluorescent molecules in deep tissue [1]. FMT systems provide functional medical imaging using non-ionizing radiation and relatively inexpensive components. A broad range of cell activity can be identified, making FMT a potentially valuable tool for cancer detection, drug discovery and gene therapy [2]. However, obstacles must be overcome before this potential can be realized; the resolution, imaging volume , and accuracy of FMT imaging is currently limited by the computational complexity of reconstruction and inaccuracies in photon propagation models. It is expected that improvements in these areas would facilitate high resolution imaging of deep structures *in vivo*, making FMT suitable for many applications.

To acquire imaging data, the tissue of interest is illuminated with laser light with a wavelength of 650-900 nm; These 'excitation' photons interact with the tissue as they travel though it, undergoing scattering and absorption interactions [1]; see Figure 1 for a simple schematic of these photon-matter interactions. For many biological tissues in this spectral window photon propagation is "scattering dominated", typically with scattering interactions several orders of magnitude more common than absorption interactions [3]. Since absorption is low in this spectral window, a significant proportion of excitation

photons travel several centimeters or more into the tissue [1]. Under such conditions of high scattering and low absorption, the transport of photons may be modeled by the diffusion approximation to radioactive transport theory [4].
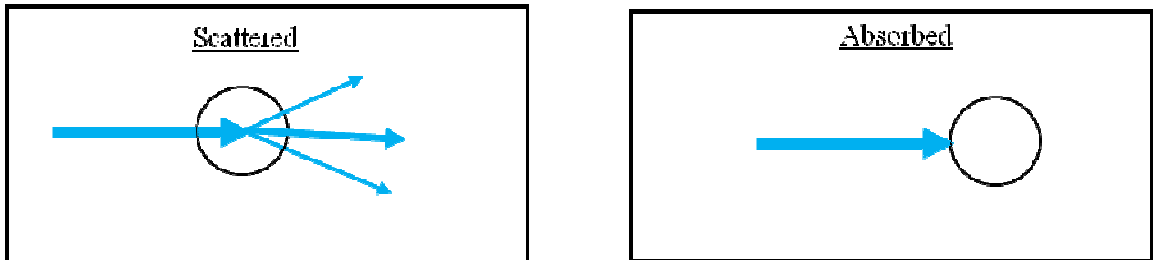
Figure 1. Photon-Matter Interactions

As the excitation photons diffuse through the media, they also interact with fluorescent molecules in the tissue; These fluorescent molecules can either be injected into the subject or be produced by the subject due to genetic modification [2]. When an excitation photon interacts with a fluorescent molecule, the excitation photon is absorbed and a 'fluorescent' photon of longer wavelength is emitted, this is shown in Figure 2. These fluorescent photons then undergo a similar diffusion-like transport through the tissue [2].
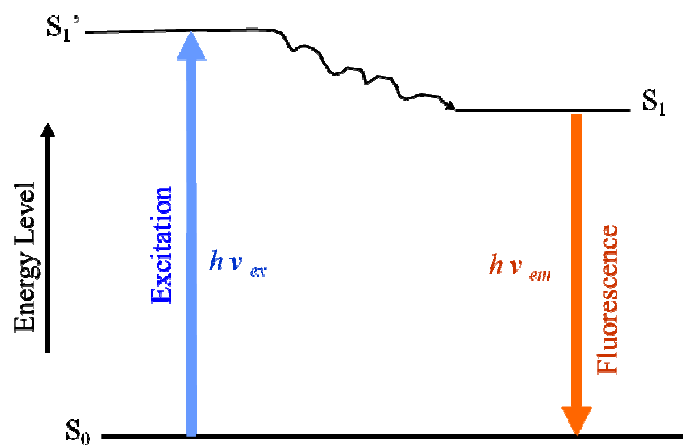
Figure 2. Simplified Jablonski Energy Diagram

Some of these fluorescent photons diffuse to the surface of the tissue, where they can be detected by direct contact detectors such as optical fibers [5] or non-contact detectors such as CCD or CMOS cameras [1] [2]. By using appropriate filters, both the intensity of fluorescent photons and excitation photons at the tissue surface can be measured. The normalized born approximation can then be calculated by dividing the intensity of fluorescent photons by that for excitation photons, leading to better experimental data by canceling out the effects of detector quantum efficiency and source strength, and reducing deviations from the model introduced by heterogeneous optical properties of the tissue [5].
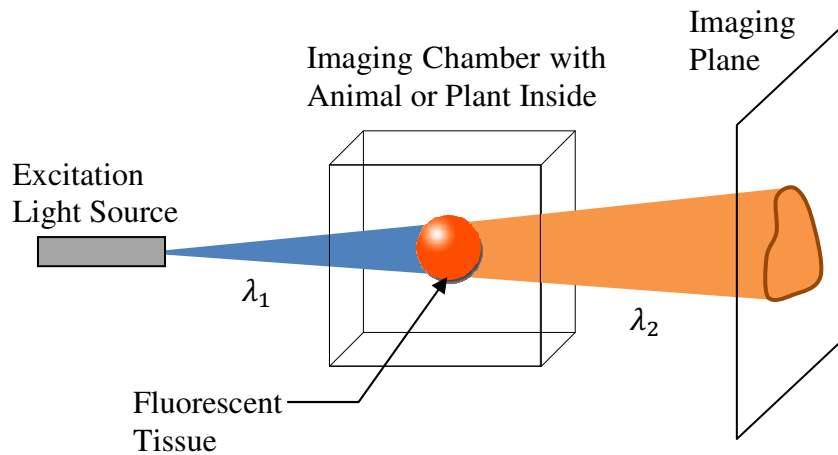
Figure 3. Simplified FMT Imaging System

By illuminating the subject with a sufficient number of sources, one at a time, and measuring the resulting fluorescent and excitation light distribution with a sufficient number of detectors, the distribution of fluorochrome inside the subject can be reconstructed. The first step in this reconstruction is to discretize the tissue volume into a set of three-dimensional volumetric pixels, also known as voxels. A model is then used

to estimate the photon propagation from each source to each voxel to each detector, this is called the forward model [1]. The data from the forward model and imaging measurements can then be written as a system of linear equations, $\underline{U}^{nB} = W \times \underline{z}$, where W is the flattened weight matrix generated by the forward model, $\underline{U}^{nB}$ is a column vector of normalized experimental measurements, and $\underline{z}$ is a column vector of the unknown fluorochrome concentrations in the voxels [2]. Solving this system of linear equations is called the inverse problem, or reconstruction, and results in an estimate of the fluorochrome concentration, $\hat{\underline{z}}$. The inverse problem for FMT is significantly more computationally intensive than for CT; the photon propagation in this wavelength window is scattering dominated, therefore filtered back projection cannot be used. Instead, typical reconstruction methods include Moore-Penrose pseudoinverse of the matrix W by singular value decomposition [2], and iterative methods such as the algebraic reconstruction technique with randomized projection order (R-ART) [1] [2].

To reduce the computational complexity of reconstruction, we decompose the forward problem into a Khatri-Rao product. Inversion of this model leads to a novel reconstruction method that significantly reduces the computational complexity and memory requirements for overdetermined datasets. Compared to the well known singular value decomposition based approach, this new reconstruction method decreases computation time by a factor of up to 25, while simultaneously reducing the memory requirement by up to three orders of magnitude. An example of an image reconstructed using this novel reconstruction method is shown in Figure 4.

4
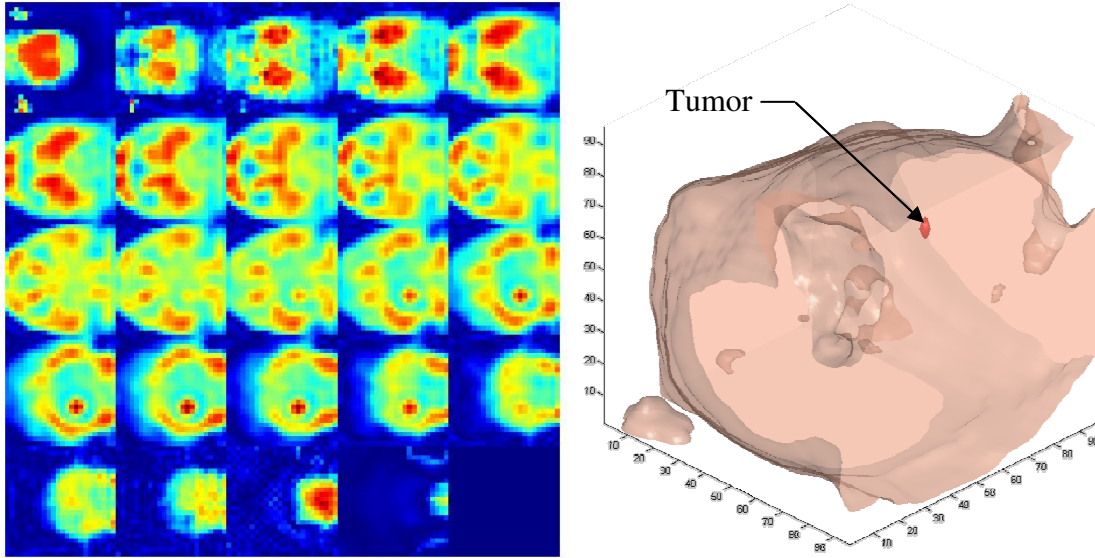
Figure 4. Reconstruction Using SVD-KR. Montage on left, 3-D rendering on right.

2. Review of Literature

2.1. Experimental Techniques for Acquiring FMT Imaging Data

The first step in collecting *in vivo* experimental imaging data typically involves introducing a fluorescent agent into the subject. This is done in one of two ways. The first method is to inject a solution containing one or more different fluorochromes into the subject shortly before imaging [2]. The fluorochrome gets distributed throughout the subject by bulk transport and diffusion, and in the process the fluorochrome interacts with and binds to its biological target. A variety of fluorochromes are commercially available; they are divided into families with different biological targets, including antibody conjugated molecular probes, nucleic acid probes, fluorescent proteins, reactive probes, and cell function probes. Alternatively, a gene that expresses a fluorescent protein can be introduced into an organism, allowing for the measurement of gene expression and regulation [2].

The next step is to collect imaging data using an FMT imaging system. Current FMT imaging systems fall into two major categories, direct contact and non-contact. In direct contact imaging systems, optical fibers used both to illuminate the tissue and measure fluorescence are in direct contact with the surface of the tissue, or paired to the surface by use of a matching fluid with optical properties similar to the tissue [2]. The advantage of direct contact imaging systems is that the shape of the tissue surface does not have to be

known or measured since the tissue is either compressed into a fixed geometry or placed in a closed container filled with liquid [1]. There are a few disadvantages to this imaging geometry; compressing the tissue into a fixed geometry distorts the natural shape, using a liquid filled chamber precludes the use of live laboratory animals, and the matching fluid induces additional photon scattering and attenuation [1].

In non-contact imaging systems, the tissue is illuminated with a laser and fluorescence is measured with a CCD camera located around the tissue. The advantages of this geometry are that large datasets from multiple angles can be acquired, and the tissue does not have to be compressed or immersed in fluid. The disadvantage of this method is that the surface shape of the tissue must be known, and inaccuracies in this measurement induce errors in the forward model [1].
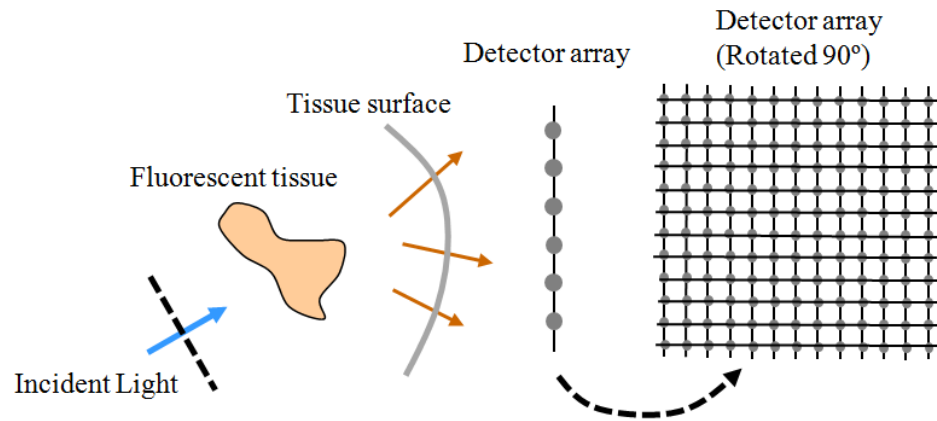
Figure 5. Simplified Non-contact FMT Imaging System

Before FMT can become a clinically useful tool, several challenges must be surmounted. First, large datasets and extensive computations are necessary to obtain a reconstruction

7

with sufficient resolution to be clinically meaningful. Second, these large datasets need to be collected quickly to minimize errors from movement of the subject and physiological changes [6].

2.2. Model for Photon Diffusion in Scattering Media

In order to accurately and quickly reconstruct an FMT image, the forward model of photon propagation has to accurately predict actual photon density in the tissue while being computationally simple. Typically, the forward model of choice is the diffusion approximation to the radiative transfer equation solved for the type of light source used in the imaging setup. The light source used in FMT is laser light either directly incident on the tissue or coupled to the tissue with an optical fiber in direct contact. In the second case the light source may be modeled as a point source. The light intensity can either be constant for steady-state measurements, frequency modulated for frequency domain measurements, or a short pulse for time-resolved measurements. The following sections review literature related to the modeling of photon diffusion in scattering media. In section 2.2.1 we discuss Dirac delta point sources, in section 2.2.2 we discuss boundary conditions, and in section 2.2.3 we discuss sinusoidally modulated point sources.

2.2.1. Dirac Delta Point Sources

Photons propagating through a scattering medium, such as tissue, scatter and attenuate as they travel. The radiative transport equation that describes this process is difficult to solve directly, so it is typically approximated by diffusion equations.   However, traditional diffusion equations assume isotropic scattering, while photon scattering   is

8

actually anisotropic. Consequently, it is assumed that after numerous anisotropic scattering events the photon distribution will be approximately isotropic. To incorporate this assumption, the scattering coefficient, μ_s, is modified by the average cosine of the angle of a scattering event, g, resulting in the reduced scattering coefficient, $\mu_s' = (1-g)\mu_s$. The photon density in the tissue $U(\vec{r}, t) \, J/mm^3$ induced by a source of photons $S(\vec{r}, t) \, W/(mm^3)$ may be found by the diffusion approximation to the radiative transfer equation [4]

$$\frac{\partial}{\partial t} U(\vec{r}, t) - vD\nabla^2 U(\vec{r}, t) + v\mu_a U(\vec{r}, t) = S(\vec{r}, t) \tag{1}$$

where, for the 3-D case,

$$\nabla^2 U = \frac{\delta^2 U}{\delta x^2} + \frac{\delta^2 U}{\delta y^2} + \frac{\delta^2 U}{\delta z^2} \tag{2}$$

and for the 2-D case,

$$\nabla^2 U = \frac{\delta^2 U}{\delta x^2} + \frac{\delta^2 U}{\delta y^2} \tag{3}$$

In (1), v is the speed of light in the tissue and has a typical value of $2.14 \times 10^{11} \, mm/s$, which corresponds to an index of refraction of $n = 1.4$, and D is the diffusion coefficient given by [4]

$$D = \frac{1}{3[\mu_a + (1-g)\mu_s]} \, mm \tag{4}$$

where μ_a is the absorption coefficient, μ_s is the scattering coefficient of the media, and g is the average cosine of the angle of a scattering event [4]. Values for these coefficients in selected components can be found in Table 1.

Table 1. Optical Properties of Tissue

Tissue	Source	μ_a mm^{-1}	$(1-g)\mu_s$ mm^{-1}	μ_s mm^{-1}	g -	D mm
Bone	Pig Skull [7]	0.04	2.625	35	0.925	0.125
Muscle	Chicken [3]	0.017	0.33	0.41	0.20	0.961
Skin	Albino Murine Dermis [3]	0.28	6.2	23.9	0.74	0.051
Lung	Human [3]	0.81	8.1	32.4	0.75	0.037
Prostate Tumor	Rat [3]	0.049	0.81	27.0	0.97	0.388
Blood	Human [3]	0.13	0.611	124.6	0.995	0.450

The diffusion equation (1) is then solved for $U(\vec{r}, t)$ at points far from sources and boundaries and for media where $\mu_a \ll (1-g)\mu_s$. For wavelengths in the $\lambda = 650$ to 900 nm range in soft tissue, this second condition is generally true [4]. The solution to (1) plotted for the 2-D case is shown in Figure 6.

$$U(\vec{r}, t) = \quad 1.\text{e-}1 \quad 1.\text{e-}2 \quad 1.\text{e-}3 \quad 1.\text{e-}4 \quad 1.\text{e-}5 \quad 1.\text{e-}6 \quad 1.\text{e-}7$$
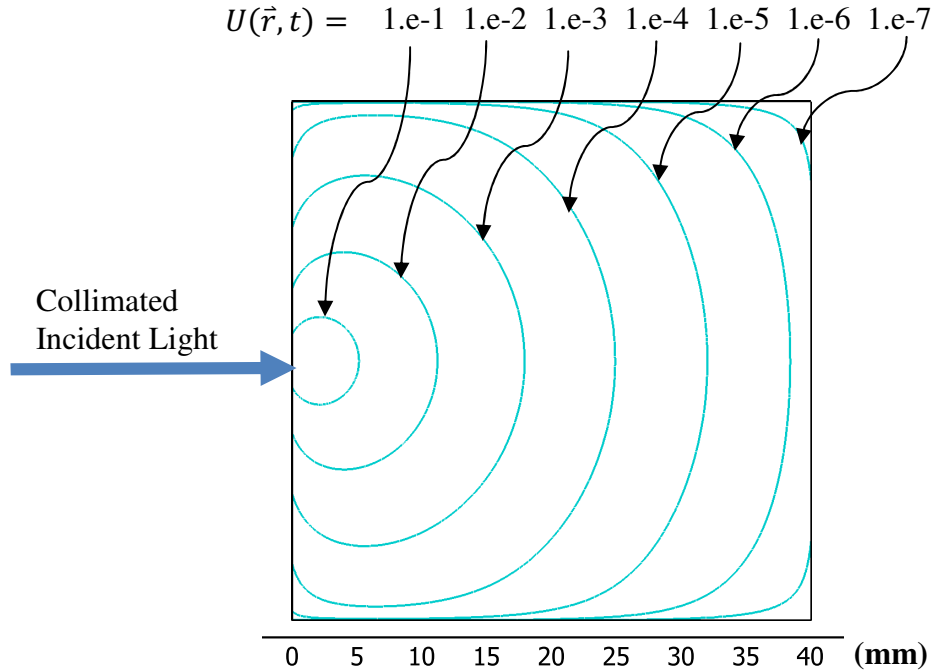
Figure 6. Solution to (1) Using COMSOL

In an infinite medium, and for an isotropic point source $S(\vec{r}_s, t) = \delta((0,0,0), 0)$, the solution to (1) becomes [4]

$$U(\vec{r}, t) = \frac{1}{(4\pi Dvt)^{3/2}} \, exp\left(-\frac{r^2}{4Dvt} - \mu_a vt\right) \tag{5}$$

where $U(\vec{r}, t)$ has units of J/mm^3, and $r = \|\vec{r}_s - \vec{r}\| = \|\vec{r}\|$ is the distance of point $\vec{r}$ from a source at $\vec{r}_s$. As an example, an isotropic source defined to be at the location $\vec{r}_s = (0,0,0)$ illuminates a sample of muscle, with optical properties found in Table 1, and $v = 3 \times 10^{11}/1.4 \ mm/s$. At a location in the muscle, $\vec{r} = (3,4,0)$, the distance would the source would be $r = \|\vec{r}_s - \vec{r}\| = \sqrt{(-3)^2 + (-4)^2} = 5$, and (5) would simplify to

$$U((3,4,0), t) = \frac{2.40 \times 10^{-19}}{t^{3/2}} \times exp\left(-\frac{3.04 \times 10^{-11}}{t} - 3.64 \times 10^9 \, t\right) \tag{6}$$

This can be plotted as a function of time, resulting in Figure 7.
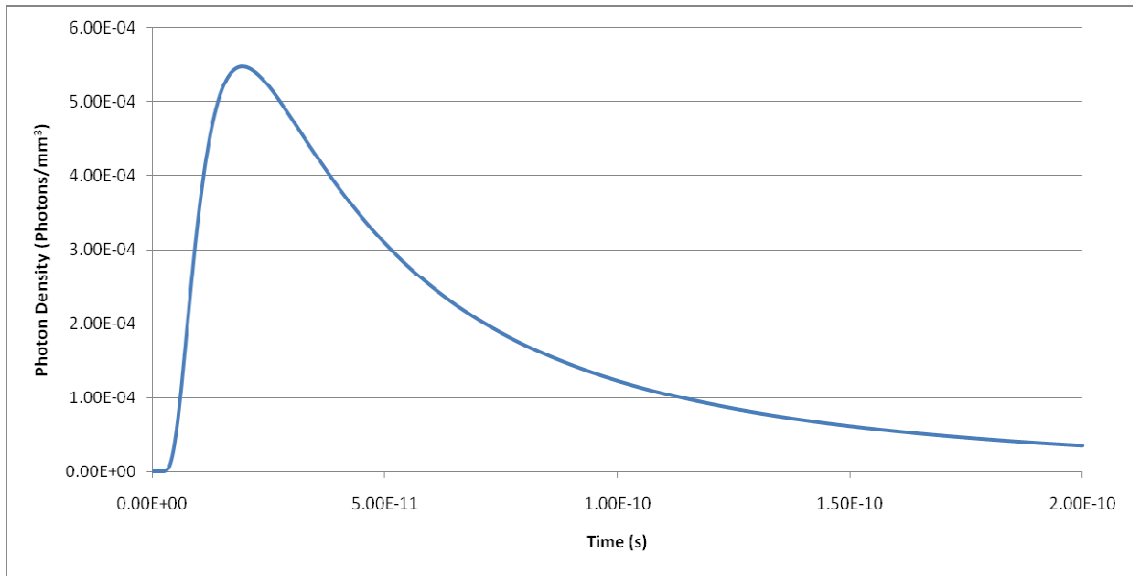
Figure 7. Photon Density vs. Time Given by (6)

In the case of fluorescence molecular tomography, the light source is anisotropic, so modifications must be made to (5). To model this situation, it is assumed that all source photons are initially scattered at a depth $z_0 = [\mu_a + (1 - g)\mu_s]^{-1}$. As shown in Figure 8, to specify a boundary condition of $U(\vec{r}, t) = 0\ J/mm^3$ at the tissue surface, a negative point source is added at $z = -z_0$ [4].
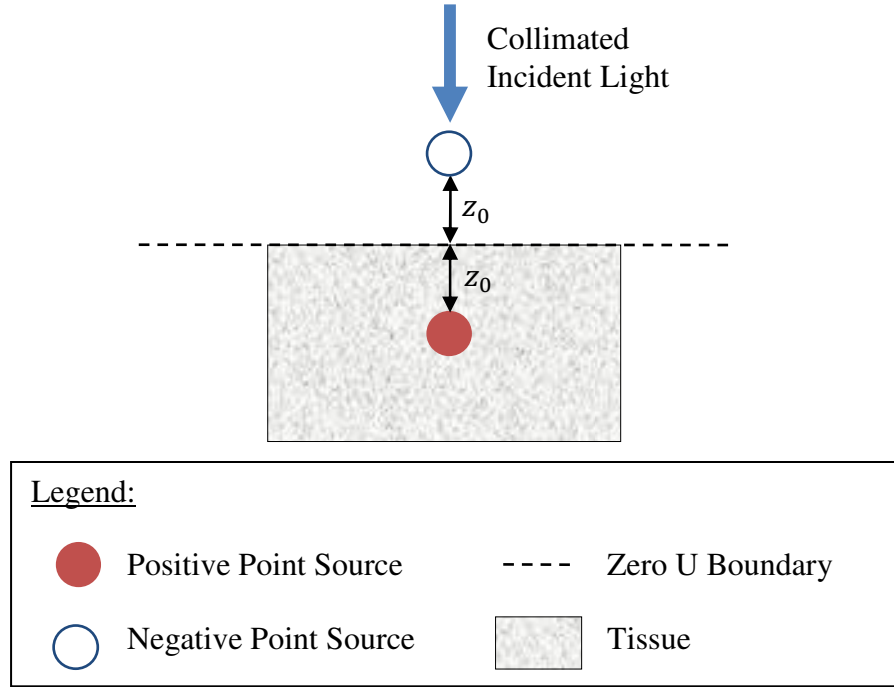
Figure 8. Model of Incident Collimated Light as Point Sources

The photon density from an anisotropic source can then be written as [4]

$$U(\vec{r}, t) = \frac{1}{(4\pi Dvt)^{3/2}}\ exp(-\mu_a vt)\left\{exp\left[-\frac{r^2}{4Dvt}\right] - exp\left[-\frac{r^2}{4Dvt}\right]\right\} \qquad (7)$$

2.2.2. Photon Diffusion Boundary Conditions

For the diffusion approximation to the radiative transfer equation, given by (1), absorbing boundaries can be modeled with a Dirichlet condition [8]

12

$$hU = g \tag{8}$$

where $h = 1, g = 0$. In contact imaging systems, boundaries between the imaging chamber and the sources or detectors are tissue-glass-air boundaries, and may be modeled with a modified Robin condition. In non-contact imaging systems, boundaries are tissue-air interfaces, which also may be modeled with a modified Robin condition [9] [8]

$$\vec{n} \cdot (v\nabla U) + hU = g \tag{9}$$

where $\vec{n}$ is the local normal vector at the boundary, $g = 0$, and [9] [8]

$$h = \frac{1}{2A} \tag{10}$$

$$A = \frac{\left[\frac{2}{1 - R_0} - 1 + |\cos\theta_c|^3\right]}{1 - |\cos\theta_c|^2} \tag{11}$$

$$R_0 = \frac{(n-1)^2}{(n+1)^2} \tag{12}$$

$$n = \frac{n_{tissue}}{n_{air}} \tag{13}$$

$$\theta_c = \sin^{-1}\left(\frac{1}{n}\right) \tag{14}$$

where θ_c is the critical angle at the boundary, n_{tissue} is the refractive index of the tissue, n_{air} is the refractive index of air, n is the relative refraction coefficient across the boundary, R_0 is the power reflection coefficient, and A is a coefficient to describe photon propagation across boundary derived from Fresnel's equations, and where for the 3-D case,

$$\nabla U = \vec{i}\frac{dU}{dx} + \vec{j}\frac{dU}{dy} + \vec{k}\frac{dU}{dz} \tag{15}$$

Alternatively, for the 2-D case,

$$\nabla U = \vec{\imath}\frac{dU}{dx} + \vec{\jmath}\frac{dU}{dy} \tag{16}$$

2.2.3. Sinusoidal Amplitude Modulated Point Sources

In subsection 2.2.1, we studied the photon diffusion approximation for Dirac delta point sources. That model is helpful for time-gated measurements, which are typically used for reflection measurements to resolve shallow structures. On the other hand, deep structures are typically resolved using transmission measurements. Transmission measurements are typically frequency domain or steady state measurements, acquired using a sinusoidally modulated or steady state light source respectively. Both situations can be modeled in highly scattering media by the results of this chapter, (29) and (30).

The photon diffusion from a isotropic sinusoidal amplitude modulated point source in a homogeneous isotropic media satisfies the Boltzmann transport equation [10],

$$\frac{\partial U(\vec{r},t)}{\partial t} + v\mu_a U(\vec{r},t) + \nabla \cdot \vec{J}(\vec{r},t) = S(\vec{r},t) \tag{17}$$

$$\nabla U(\vec{r},t) + \frac{\partial}{\partial t}\frac{3\vec{J}(\vec{r},t)}{v^2} + \frac{\vec{J}(\vec{r},t)}{vD} = 0 \tag{18}$$

where $U(\vec{r},t)$ is the photon density with units J/mm^3, $\vec{J}(\vec{r},t)$ is the photon current density with units W/mm^2, and D is the diffusion coefficient given above by (4). The relationship between $U(\vec{r},t)$ and $\vec{J}(\vec{r},t)$ will be given later. $U(\vec{r},t)$ and $\vec{J}(\vec{r},t)$ can be accurately determined for points far from sources or boundaries in media where $\mu_a \ll \mu_s$ [10]. A sinusoidal isotropic point photon source is given by [10]

14

$$S(\vec{r}_s, t) = \delta(\vec{r}_s)\{A_{dc} + A_{ac}\, exp[-j\omega t]\} \tag{19}$$

where A_{ac} is the amplitude of frequency-dependant source modulation, A_{dc} is the amplitude of dc source intensity where $A_{dc} \geq A_{ac}$, and ω is the angular frequency of the source modulation. It is assumed that $U(\vec{r}, t)$ and $\vec{J}(\vec{r}, t)$ have the following forms [10]:

$$U(\vec{r}, t) = [U(\vec{r})]_{dc} + [U(\vec{r})]_{ac}\, exp[-j(\omega t + \alpha)] \tag{20}$$

$$\vec{J}(\vec{r}, t) = [\vec{J}(\vec{r})]_{dc} + [\vec{J}(\vec{r})]_{ac}\, exp[-j(\omega t + \beta)] \tag{21}$$

where α and β are phase angles. Substituting (19) into (17), and using the above forms for $U(\vec{r}, t)$ and $\vec{J}(\vec{r}, t)$ results in the steady-state and frequency-dependent equations for $U(\vec{r})$ and $\vec{J}(\vec{r})$ [10],

$$v\mu_a\, [U(\vec{r})]_{dc} + \nabla \cdot [\vec{J}(\vec{r})]_{dc} = A_{dc}\, \delta(\vec{r}) \tag{22}$$

$$[\vec{J}(\vec{r})]_{dc} = -vD\nabla[U(\vec{r})]_{dc} \tag{23}$$

$$(v\mu_a - j\omega)[U(\vec{r})]_{ac} + \nabla \cdot [\vec{J}(\vec{r})]_{ac} = A_{ac}\delta(\vec{r}) \tag{24}$$

$$[\vec{J}(\vec{r})]_{ac} = -vD \left[\frac{1 + j3\omega D/v}{1 + (3\omega d/v)^2}\right] \nabla[U(\vec{r})]_{ac} \tag{25}$$

By making the assumption that $D \ll v/\omega$, which is equivalent to making the assumption that the mean free path between scattering events is much shorter than the wavelength of the sinusoidal modulation, (25) reduces to [10]

$$[\vec{J}(\vec{r})]_{ac} \cong -vD\nabla[U(\vec{r})]_{ac} \tag{26}$$

where $\vec{J}(\vec{r})$ has units of W/mm^2 and $U(\vec{r})$ has units of J/mm^3. By combining (22) and (23) to eliminate $[\vec{J}(\vec{r})]_{dc}$, results in [10]

$$\nabla^2[U(\vec{r})]_{dc} - \frac{\mu_a}{D}[U(\vec{r})]_{dc} = -\frac{A_{dc}}{vD}\delta(\vec{r}) \tag{27}$$

Likewise, combining (25) and (26) to eliminate $[\vec{J}(\vec{r})]_{ac}$, results in [10]

$$\nabla^2[U(\vec{r})]_{ac} - \left(\frac{v\mu_a - j\omega}{vD}\right)[U(\vec{r})]_{ac} = -\frac{A_{ac}}{vD}\delta(\vec{r}) \tag{28}$$

It is worth noting that (27) and (28) are the steady-state and frequency domain equivalents of (1) respectively. (27) and (28) can be solved for an infinite media, resulting in [10]

$$
\begin{aligned}
U(\vec{r},t) = {} & \frac{A_{dc}}{4\pi vDr}\,exp\left[-r\sqrt{\frac{\mu_a}{D}}\right] + \frac{A_{ac}}{4\pi vDr} \\[6pt]
& \times exp\left\{-r\left(\frac{v^2\mu_a{}^2 + \omega^2}{v^2D^2}\right)^{1/4} cos\left[\frac{1}{2}\tan^{-1}\left(\frac{\omega}{v\mu_a}\right)\right]\right\} \\[6pt]
& \times exp\left\{jr\left(\frac{v^2\mu_a{}^2 + \omega^2}{v^2D^2}\right)^{1/4} sin\left[\frac{1}{2}\tan^{-1}\left(\frac{\omega}{v\mu_a}\right)\right]\right. \\[6pt]
& \left. - j(\omega t + \theta)\right\}
\end{aligned}
\tag{29}
$$

This equation is the frequency domain equivalent of (5). For the case where $\mu_a \approx 0$, (29) simplifies to [10]

$$
\begin{aligned}
U(\vec{r},t) = {} & \frac{A_{dc}}{4\pi vDr} + \frac{A_{ac}}{4\pi vDr} \times exp\left[-r\sqrt{\frac{\omega}{2vD}}\right] \\[6pt]
& \times exp\left[jr\sqrt{\frac{\omega}{2vD}} - j(\omega t + \theta)\right]
\end{aligned}
\tag{30}
$$

As an example, an isotropic steady-state source, with $A_{dc} = 10^{20}$, $A_{ac} = 5 \times 10^{19}$, $\omega = 10^7/sec$, $\theta = 0$, and defined to be at the location $\vec{r}_s = (0,0,0)$, illuminates a sample of muscle, with optical properties found in Table 1 and $v = 3 \times 10^{11}/1.4\ mm/s$. At a

16

location in the muscle, $\vec{r} = (3, 4, 0)$, the distance to the source would be $r = \|\vec{r}_s - \vec{r}\| =$

$\sqrt{(-3)^2 + (-4)^2} = 5$, and (30) would simplify to

$$U(\vec{r}, t) = 7.729 \times 10^6 + 3.770 \times 10^6 \times exp[j(0.0246 - 10^7 t)] \tag{31}$$

Plotting $|U(\vec{r}, t)|$ as a function of time results in Figure 9.
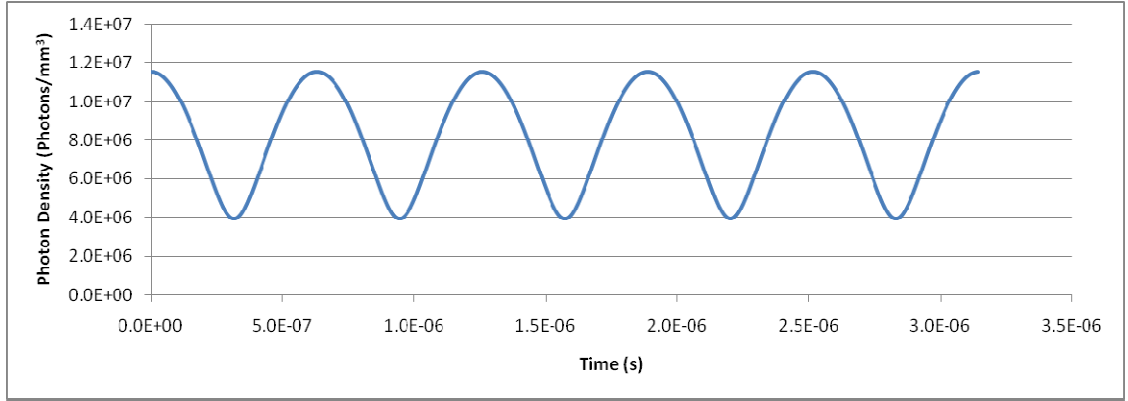
Figure 9. Magnitude of Photon Density vs. Time for Example (31)

Alternatively, when $\omega = 0$, (29) simplifies to the steady state solution,

$$U(\vec{r}) = \frac{A_{dc}}{4\pi v D r} exp\left[-r\sqrt{\frac{\mu_a}{D}}\right] \tag{32}$$

As an example, an isotropic steady-state source, with $A_{dc} = 10^{20}$ and defined to be at the location $\vec{r}_s = (0, 0, 0)$, illuminates a sample of muscle, with optical properties found in Table 1 and $v = 3 \times 10^{11}/1.4 \; mm/s$. At a location in the muscle, $\vec{r} = (3, 4, 0)$, the distance to the source would be $r = \|\vec{r}_s - \vec{r}\| = \sqrt{(-3)^2 + (-4)^2} = 5$, and (32) would simplify to

$$U(3, 4, 0) = \frac{10^{20}}{4\pi \left(\frac{3 \times 10^{11}}{1.4}\right)(0.961)(5)} exp\left(-5\sqrt{\frac{0.017}{0.961}}\right) = 3.98 \times 10^6 \tag{33}$$

17

2.3. Normalized Born Field

The forward problem for FMT involves not only photon propagation through a media, but also photon interaction with fluorochromes. To model this combined forward problem a Born-field approximation can be used. Noting from (30) that the photon density attenuates with the form $exp(-\alpha r)/r$, and can be represented in the frequency domain in the following simplified form [5]:

$$U_0(\vec{r}_s, \vec{r}, \omega) = \frac{\Theta_s(\vec{r}_s) \, exp \, (jkr)}{4\pi v D r} \tag{34}$$

where $U_0(\vec{r}_s, \vec{r}, \omega)$ has units of J/mm^3 and is the photon density at position $\vec{r}$ due to a source at $\vec{r}_s$ with modulation angular frequency ω, $\Theta_s(\vec{r}_s)$ is the source gain factor, $k = [(v\mu_a + j\omega)/(vD)]^{1/2} \, mm^{-1}$ is the scalar propagation constant, $r = \|\vec{r}_s - \vec{r}\|$ is the distance from the source, and $D = [3(\mu_a + (1-g)\mu_s)]^{-1} \, mm$. Building upon this equation, the detected intensity of excitation wavelength light at a detector located at $\vec{r}_d$ due to a source located at $\vec{r}_s$ is given by [5]

$$U_{inc}(\vec{r}_s, \vec{r}_d) = \eta^{\lambda 1} \times \Theta_s(\vec{r}_s) \times \Theta_d(\vec{r}_d) \times U_0(\vec{r}_s, \vec{r}_d, k^{\lambda 1}) \tag{35}$$

where $\eta^{\lambda 1}$ is the quantum efficiency of the detector for at wavelength λ_1, $\Theta_d(\vec{r}_d)$ is the detector gain factor, $k^{\lambda 1}$ is the wave propagation constant for excitation wavelength light, and λ_1 is the wavelength of excitation light and has a typical value of 672 nm [1]. The intensity of fluorescence wavelength light detected at a detector located at $\vec{r}_d$ due to the fluorochrome distribution $z(\vec{r})$ illuminated by a source located at $\vec{r}_s$, is given by [5]

18

$$U_{fl}(\vec{r}_s, \vec{r}_d) = \iiint \Theta_s(\vec{r}_s) \times \Theta_f \times \eta^{\lambda 2} \times \Theta_d(\vec{r}_d) \times U_0(\vec{r}_s, \vec{r}, k^{\lambda 1})$$

$$\times \frac{z(\vec{r})}{1 - j\omega\tau(\vec{r})} \times \frac{v}{D^{\lambda 2}} \times U_0(\vec{r}, \vec{r}_d, k^{\lambda 2}) \ d^3\vec{r}$$

(36)

where $z(\vec{r})$ is the distribution of fluorophore in the media with units mm^{-3}, $\tau(\vec{r})$ is the fluorescence time constant with units of seconds, $k^{\lambda 2}$ is the wave propagation vector for the fluorescent wavelength, Θ_f is the attenuation of the filter used to select for detection only fluorescent light, and $\eta^{\lambda 2}$ is the quantum efficiency of the detector for fluorescent wavelength light. λ_2 is the wavelength of fluorescent light and has a typical value of 710 nm [1]. Since $\Theta_s(\vec{r}_s)$ and $\Theta_d(\vec{r}_d)$, the source and detector gain, are position dependent, finding a solution to (35) and (36) would require measurement of these values for each pair of sources and detectors. To reduce the experimental measurements required, (35) and (36) can be combined to eliminate these terms resulting in the normalized born field equation [5],

$$U^{nB}(\vec{r}_s, \vec{r}_d) = \frac{1}{\Theta_f} \times \frac{U_{fl}(\vec{r}_s, \vec{r}_d)}{U_{inc}(\vec{r}_s, \vec{r}_d)} \times \frac{\eta^{\lambda 1}}{\eta^{\lambda 2}}$$

(37)

By assuming that $\eta^{\lambda 1} \approx \eta^{\lambda 2}$ due to the similarity of these wavelengths in FMT imaging systems, and combining (37) with (35) and (36), yields [5]

$$U^{nB}(\vec{r}_s, \vec{r}_d) = \frac{1}{U_0(\vec{r}_s, \vec{r}_d, k^{\lambda 1})}$$

$$\times \iiint U_0(\vec{r}_s, \vec{r}, k^{\lambda 1}) \times \frac{z(\vec{r})}{1 - j\omega\tau(\vec{r})} \times \frac{v}{D^{\lambda 2}}$$

(38)

$$\times U_0(\vec{r}, \vec{r}_d, k^{\lambda 2}) \ d^3\vec{r}$$

This equation is an approximation of the normalized born field. In the section that follows, this equation will be used to generate the weight matrix in the forward problem.

2.4. Reconstruction Methods

The inverse problem for FMT requires solving the following equation [2]:

$$\underline{U}^{nB} = W \times \underline{z} \tag{39}$$

where $\underline{U}^{nB}$ is the measurement vector given by (38), W is the weight matrix relating each measurement to each voxel of fluorochrome, and $\underline{z}$ is the fluorochrome concentration column vector. In (39), $\underline{U}^{nB}$ has units J/mm^2, W has units J/mm^2, and $\underline{z}$ has units mm^{-3}; while this might seem unbalanced at first glance, the matrix multiplication is performing a summation over three spatial dimensions, leading to the correct balance of units. For the steady-state case, where $\omega = 0$, W is calculated using the right side of (38), as shown in the following equation [2]:

$$W(\vec{r}_s, \vec{r}_d, \vec{r}) = \frac{v}{D^{\lambda 2}} \times \frac{U_0(\vec{r}_s, \vec{r}, k^{\lambda 1}) \times U_0(\vec{r}, \vec{r}_d, k^{\lambda 2})}{U_0(\vec{r}_s, \vec{r}_d, k^{\lambda 1})} \tag{40}$$

where W is typically a 2-D matrix, and for each element W_{ij}, each i is a unique source detector pair, and each j is a unique voxel in the volume to be imaged.
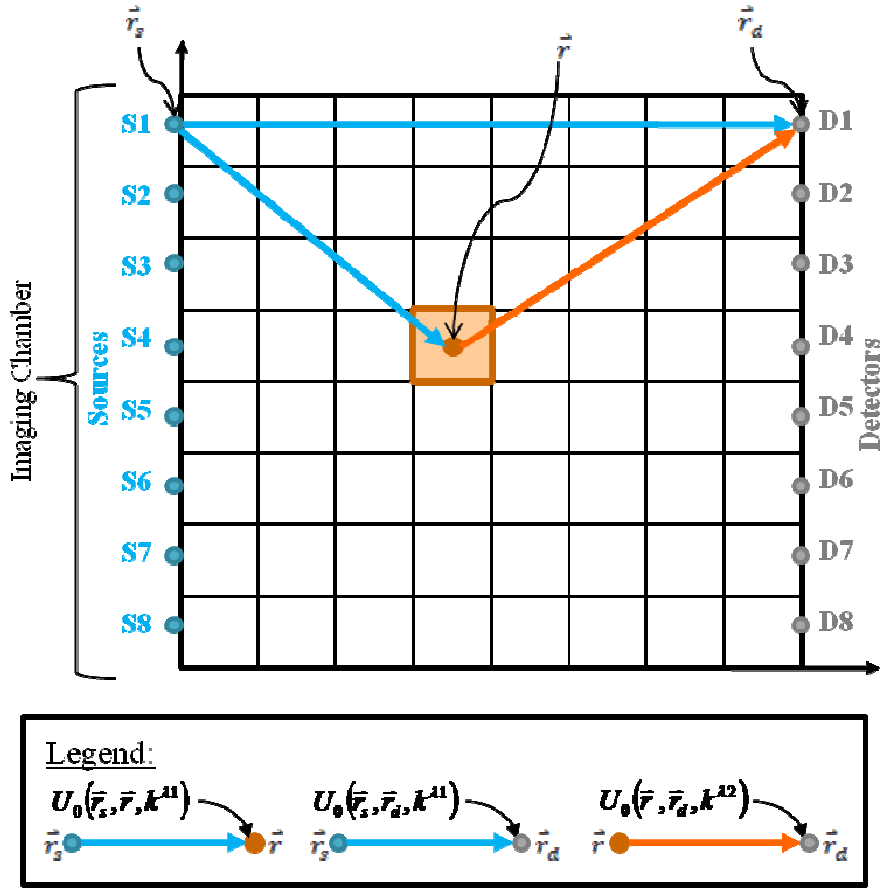
Figure 10. Calculation of Weight Matrix for Simplified 2-D FMT System

An example of how one element of this matrix would be calculated for a simple 2-D system is shown in Figure 10; it is important to note that the tip of each vector represents the location of the annotated U_0.

The system of equations shown in (39) can be solved for $\hat{\underline{z}}$, the estimated fluorochrome concentration vector, when $\underline{U}^{nB}$ is determined experimentally and W is calculated using (40). There are multiple methods for solving this system of equations. Graves (2003) used an iterative method called the method of projections, also known as the algebraic reconstruction technique with randomized projection order (R-ART). In the method of

projections, each row vector of W and its corresponding value of $\underline{U}^{nB}$ defines an affine hyperplane. The guess for the value of $\underline{\hat{z}}^{(i)}$ is updated each iteration by projecting the previous guess, $\underline{\hat{z}}^{(i-1)}$, onto an affine hyperplane using the following formula [11]:

$$\underline{\hat{z}}^{(i)} = \underline{\hat{z}}^{(i-1)} - \frac{\underline{\hat{z}}^{(i-1)} \cdot \underline{w_i} - U_i^{nB}}{\underline{w_i} \cdot \underline{w_i}} \times \underline{w_i} \tag{41}$$

where $\underline{\hat{z}}^{(i)}$ is the fluorochrome vector after the projection, $\underline{\hat{z}}^{(i-1)}$ is the fluorochrome vector before the projection, $\underline{w_i}$ is the ith row of the matrix W, and U_i^{nB} is the ith element in the $\underline{U}^{nB}$ measurement vector. Figure 11 shows an example of the method of projections for solving a system of two equations and two unknowns. An initial guess is projected onto a hyperplane, and the resulting point is projected onto the other hyperplane; this is repeated until convergence to within a specified tolerance is achieved.
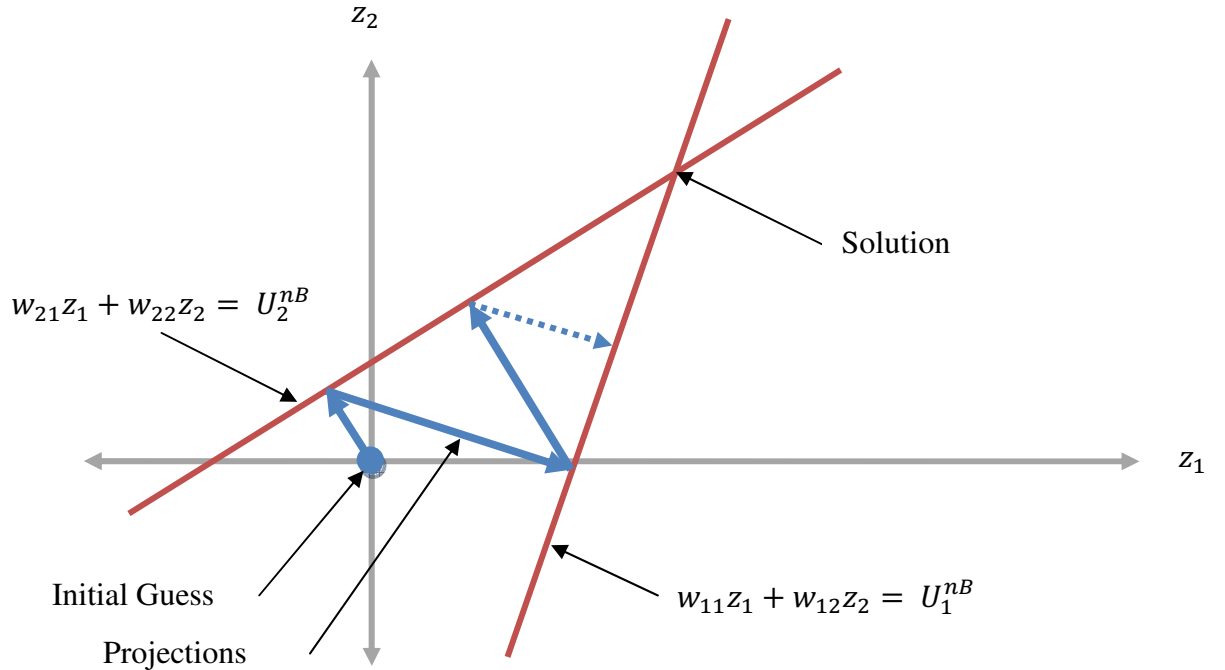
Figure 11. Method of Projections for Two Equations and Two Unknowns

Alternatively the Moore-Penrose pseudoinverse of the matrix W can be found using singular value decomposition to obtain a direct solution for $\underline{z}$ [2]. This method requires finding the singular value decomposition of the matrix W [2],

$$W = USV^T \tag{42}$$

where U and V are orthogonal basis matrices and S is a diagonal matrix that contains the singular values. Using the above singular value decomposition, a solution for (39) can be obtained:

$$\hat{\underline{z}} = W^+\underline{U}^{nB} = VS^{-1}U^T\,\underline{U}^{nB} \tag{43}$$

where W^+ is the Moore-Penrose pseudoinverse of W. To enhance the accuracy of the reconstruction from noisy measurements, singular values below a certain threshold are typically discarded [2].

For a reconstruction of an N x N x N voxel volume, the minimum size of the matrix W is N^3 by N^3. As an example, for $N = 32$, the minimum size of the matrix W would be $32,768$ by $32,768$, for $N = 64$ this increases to $262,144$ by $262,144$. To obtain better reconstructions with noisy measurements more imaging data than this minimum value is typically collected, making the system overdetermined. Solving systems of equations with such a large number of equations and unknowns requires a considerable number of computations and large amounts of memory.

3. Challenges in FMT Reconstruction

Past reconstructions of FMT images have been limited by memory and computational constraints to a relevantly small number of source-detector pairs, and consequently are restricted to relatively low spatial sampling. To overcome these limitations, the formulation of the forward problem was decomposed into a diagonal matrix multiplied by a Khatri-Rao product. For overdetermined cases, this decomposition significantly reduces the computational and memory complexity of reconstruction; this allows for larger imaging datasets with more source-detector pairs and higher spatial sampling. Higher spatial sampling has been shown to allow higher reconstruction resolution, improve the signal to noise ratio of measurements, and improve reconstruction image quality [12]. Additionally, for overdetermined datasets - those with more source-detector pairs than reconstruction voxels - this method significantly reduces the computational complexity of reconstruction compared to method of projections reconstructions and the memory complexity of reconstruction when compared to SVD based Moore-Penrose pseudoinverse reconstructions. The performance of this algorithm will be compared against these reconstruction methods.

The reconstruction of FMT images is an ill-posed problem, with a poorly conditioned weight matrix. Consequently, small errors in the forward model can create significantly larger errors in the reconstructed image. Improving the prediction accuracy of photon

propagation in the forward model would therefore allow for significant increases in the accuracy and image quality of FMT reconstructions.

4. FMT Reconstruction Via Khatri-Rao Decomposition

Large measurement datasets are necessary to obtain reconstruction with sufficient resolution to be clinically meaningful. However, the computational complexity of reconstructing large datasets can be prohibitive. To reduce the computational complexity of reconstruction, the forward problem weight matrix, (40), was decomposed into a product of smaller matrices. This reformulation of the forward problem significantly reduces the computational complexity of reconstructing overdetermined datasets.

4.1. Theory

4.1.1. Weight Matrix in Tensor and Array Forms

The weight matrix relates the experimental measurements of each source and detector pair in the imaging system to the concentration of fluorochrome in each voxel. The weight matrix is generated by a forward model. The forward model used here is the normalized Born equation, given by (40); however the following method can be used for any forward model in imaging systems where every source contributes to the detected signal at every detector. Each element of the weight matrix specifies a unique source-voxel-detector combination, and is calculated as shown in Figure 10 and (40).

Although the matrix W is shown as a three dimensional tensor in (40), for reconstruction purposes the matrix is typically flattened to a two dimensional array of size m by n where

26

m is the number of source-detector pairs and n is the number of voxels being reconstructed,

$$W(\vec{r}_s, \vec{r}_d, \vec{r}) \xrightarrow{Flatten} W(\vec{r}_{sd}, \vec{r}) \qquad (44)$$

Flattening the matrix W can be represented graphically:
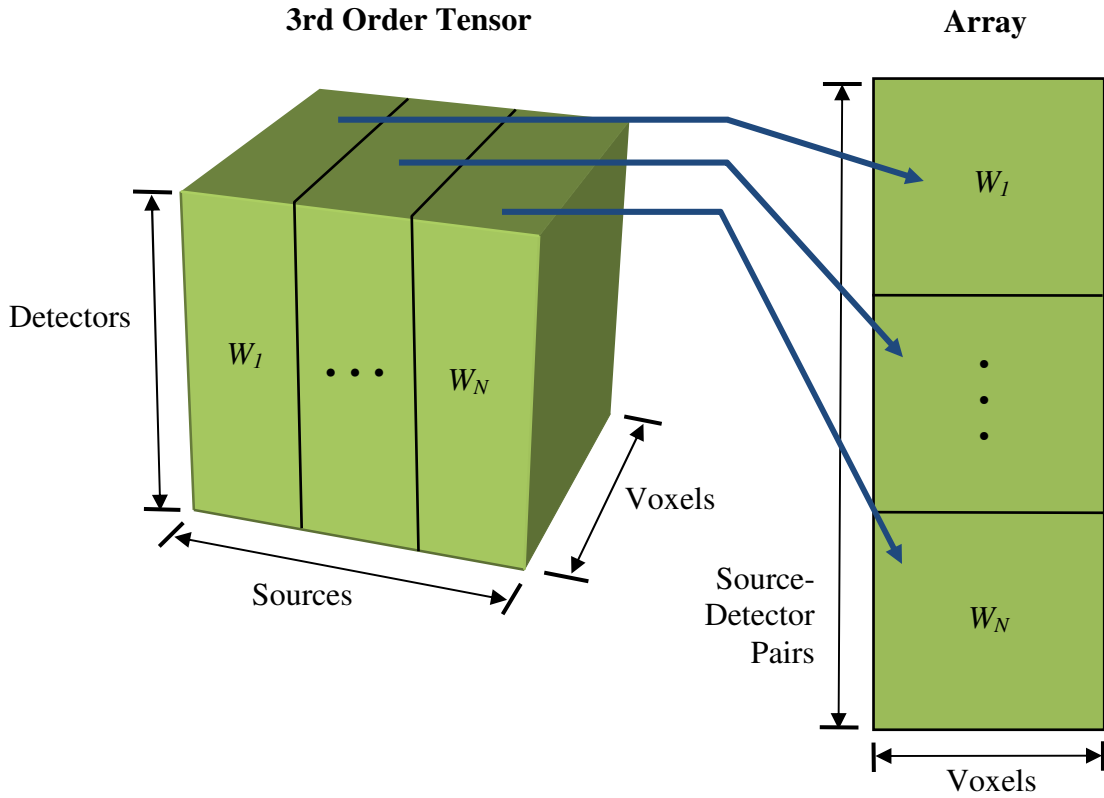
Figure 12. Flattening the Weight Matrix from a Tensor to an Array

4.1.2. Decomposition of Weight Matrix to Extract Normalizing Term

When the matrix W is flattened, the normalizing term $U_0\left(\vec{r}_s, \vec{r}_d, k^{\lambda 1}\right)$ becomes a constant for each row, $W(\vec{r}_{sd}, :)$. Consequently, the matrix W can be expressed as a constant times the matrix product of a diagonal matrix W_{nB} to the left of W_{sd}, the non-normalized

matrix W,

$$W = \frac{v}{D^{\lambda 2}} \, W_{nB} \, W_{\text{sd}} \tag{45}$$

where the diagonal entries of W_{nB} are

$$W_{nB}(\vec{r}_{sd}) = \frac{1}{U_0(\vec{r}_s, \vec{r}_d, k^{\lambda 1})} \tag{46}$$

The non-diagonal entries are equal to zero. This decomposition can be represented graphically as:

$$W \qquad\qquad W_{nB} \qquad\qquad W_{sd}$$

Full matrix
(arrows represent
rows $W(\vec{r}_{sd}, :)$)

Diagonal matrix
(arrow represents
nonzero elements)

Full matrix
(arrows represent
rows $W_{sd}(\vec{r}_{sd}, :)$)
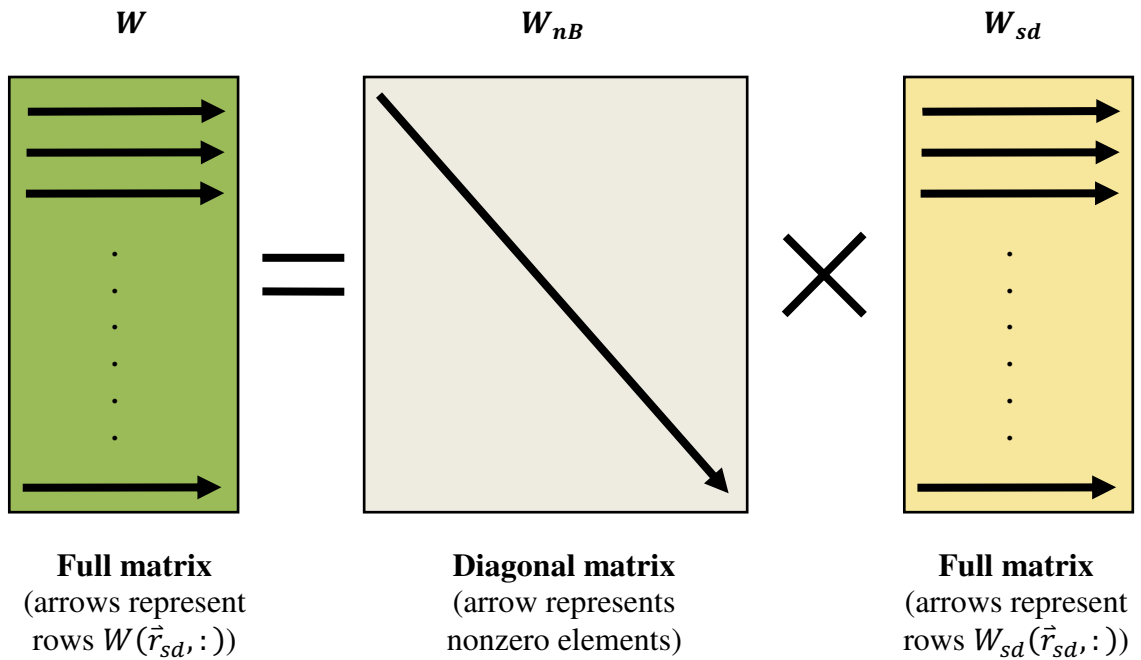
Figure 13. Decomposition of Weight Matrix to Remove Normalizing Term

In general, if this method is used for a different forward model which does not have a normalization term, W_{nB} would be equal to the identity matrix, I, and this step can be omitted entirely.

4.1.3. Decomposition of Weight Matrix to Khatri-Rao Product

W_{sd}, the non-normalized matrix W, can be decomposed to be expressed as a Kronecker-like product of two smaller matrices. Before discussing this decomposition in detail, some basic information on the Kronecker product and Khatri-Rao product is provided below.

Given two matrices A and B, each of size 2 by 2, the Kronecker product of A and B is equal to

$$A \otimes B = \begin{bmatrix} a_{11}B & a_{12}B \\ a_{21}B & a_{22}B \end{bmatrix} = \begin{bmatrix} a_{11}b_{11} & a_{11}b_{12} & a_{12}b_{11} & a_{12}b_{12} \\ a_{11}b_{21} & a_{11}b_{22} & a_{12}b_{21} & a_{12}b_{22} \\ a_{21}b_{11} & a_{21}b_{12} & a_{22}b_{11} & a_{22}b_{12} \\ a_{21}b_{21} & a_{21}b_{22} & a_{22}b_{21} & a_{22}b_{22} \end{bmatrix} \tag{47}$$

where $\otimes$ is the Kronecker operator. More generally, if A and B are of size m_a by n_a and m_b by n_b respectively, the Kronecker product of A and B results in a matrix of size $m_a\, m_b$ by $n_a\, n_b$ formed by multiplying each element in A by every element in B [13].

The Khatri-Rao (KR) product, also called the column wise Kronecker product, is a matrix operation that is related to the Kronecker product. Given two matrices C and D of size m_c by n and m_d by n, the KR product is defined as [13]

$$C \odot D = \begin{bmatrix} c_{:1} \otimes d_{:1} & c_{:2} \otimes d_{:2} & \cdots & c_{:n} \otimes d_{:n} \end{bmatrix} \tag{48}$$

where $\odot$ is the KR operator. The resulting matrix is of size $m_c\, m_d$ by n and is a subset of the columns of $C \otimes D$ [13]. For matrices C and D each of size 2 by 2, their KR product is equal to

$$C \odot D = \begin{bmatrix} c_{11}d_{11} & c_{12}d_{12} \\ c_{11}d_{21} & c_{12}d_{22} \\ c_{21}d_{11} & c_{22}d_{12} \\ c_{21}d_{21} & c_{22}d_{22} \end{bmatrix} \tag{49}$$

Note that the matrices C and D must have the same number of columns.

W_{sd}, can be decomposed to be expressed as a KR product of the matrices W_s and W_d,

$$W_{sd} = W_s \odot W_d \tag{50}$$

where

$$W_s(\vec{r}_s, \vec{r}) = U_0(\vec{r}_s, \vec{r}, k^{\lambda 1}) \tag{51}$$

$$W_d(\vec{r}_d, \vec{r}) = U_0(\vec{r}, \vec{r}_d, k^{\lambda 2}) \tag{52}$$

(50) can be represented graphically as shown in Figure 14, for a reconstruction of an n voxel image from an imaging system with m_s sources and m_d detectors.

Full matrix
Size: $m_s m_d$ by n
(arrows represent
columns $W_{sd}(:, \vec{r})$)

Full matrix
Size: m_s by n
(arrows represent
columns $W_s(:, \vec{r})$)

Full matrix
Size: m_d by n
(arrows represent
columns $W_d(:, \vec{r})$)
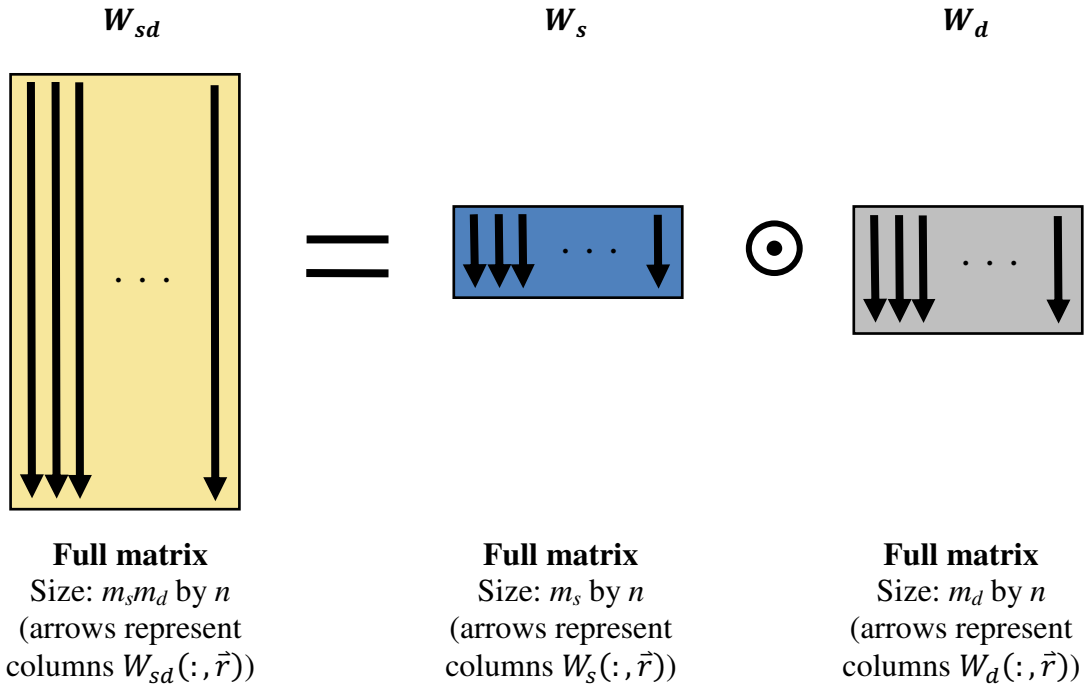
Figure 14. KR Product Decomposition of W_{sd}

By combining (45) and (50), W can be rewritten as

$$W = \frac{v}{D^{\lambda 2}} W_{nB} [W_s \odot W_d] \tag{53}$$

4.1.4. Pseudoinverse of Khatri-Rao Product

From (53), the Moore-Penrose pseudoinverse of W can be written as

$$W^+ = \frac{D^{\lambda 2}}{v} [W_s \odot W_d]^+ W_{nB}^{-1} \tag{54}$$

where W_{nB} is given by (46), W_s is given by (51), W_d is given by (52). The inverse of W_{nB}, since it is a diagonal matrix, is the element-wise inverse of each non-zero element in the matrix. A simple example of the inverse of a diagonal matrix such as W_{nB} is

$$W_{nB} = \begin{bmatrix} 4 & 0 & 0 \\ 0 & 2 & 0 \\ 0 & 0 & 0.5 \end{bmatrix} \overset{inverse}{\Longleftrightarrow} W_{nB}^{-1} = \begin{bmatrix} 0.25 & 0 & 0 \\ 0 & 0.5 & 0 \\ 0 & 0 & 2 \end{bmatrix} \tag{55}$$

The following identity is then applied to the pseudoinverse of a KR product shown in (54); given matrices A and B [13],

$$(A \odot B)^T (A \odot B) = (A^T A) \circledast (B^T B) \tag{56}$$

where $\circledast$ is the Hadamard operator, also known as the element-wise multiplication operator, defined as

$$E \circledast F = \begin{bmatrix} e_{11} & e_{12} \\ e_{21} & e_{22} \end{bmatrix} \circledast \begin{bmatrix} f_{11} & f_{12} \\ f_{21} & f_{22} \end{bmatrix} = \begin{bmatrix} e_{11}f_{11} & e_{12}f_{12} \\ e_{21}f_{21} & e_{22}f_{22} \end{bmatrix} \tag{57}$$

(56) can be rewritten as [13]

$$(A \odot B)^+ = \{(A^T A) \circledast (B^T B)\}^+ (A \odot B)^T \tag{58}$$

(58) can be substituted into (54) for $A = W_s$, and $B = W_d$, resulting in

31

$$W^+ = \frac{D^{\lambda 2}}{v} \left[\left\{ (W_s{}^T W_s) \circledast (W_d{}^T W_d) \right\}^+ (W_s \odot W_d)^T \right] W_{nB}{}^{-1} \tag{59}$$

This is a new result to the best of my knowledge. As will be discussed shortly, this result can significantly reduce the reconstruction computational complexity and memory requirements for reconstruction when the matrix W is overdetermined.

4.2. Reconstruction Algorithms

By combining (42) and (59), the following equation for the reconstructed fluorochrome concentration, $\underline{\hat{z}}$, is obtained:

$$\underline{\hat{z}} = W^+ \underline{U}^{nB} = \frac{D^{\lambda 2}}{v} \left\{ (W_s{}^T W_s) \circledast (W_d{}^T W_d) \right\}^+ (W_s \odot W_d)^T W_{nB}{}^{-1} \underline{U}^{nB} \tag{60}$$

Recall that W_{nB} is given by (46), W_s is given by (51), W_d is given by (52), and $\circledast$ is the Hadamard operator given by (59). To simplify the notation in the following discussion, (59) will be rewritten as

$$\underline{\hat{z}} = A^+ \underline{b} \tag{61}$$

where

$$A = \left\{ (W_s{}^T W_s) \circledast (W_d{}^T W_d) \right\} \tag{62}$$

$$\underline{b} = \frac{D^{\lambda 2}}{v} (W_s \odot W_d)^T W_{nB}{}^{-1} \underline{U}^{nB} \tag{63}$$

For an imaging system with m_s sources and m_d detectors, for a total of $m = m_s \times m_d$ source-detector pairs, and with n voxels in the forward model, both the matrix W^+ and $(W_s \odot W_d)^T$ are of size n by m. For overdetermined systems with $m \gg n$ these matrices can become prohibitively large, requiring significant amounts of memory to store. Consequently, a reconstruction method that does not require these matrices to be

32

stored in memory could significantly reduce the memory complexity of the problem. Two different reconstruction algorithms that satisfy this criteria were investigated. Both methods involve reconstruction by taking the singular value decomposition of a matrix generated from a KR product, this method will be called SVD-KR reconstruction for short.

4.2.1. Method 1: Row-Wise SVD-KR Reconstruction

In this reconstruction method, one row at a time of the matrix $(W_s \odot W_d)^T$ is calculated and multiplied by the pre-computed vector $\frac{D^{\lambda 2}}{v} W_{nB}^{-1} \underline{U}^{nB}$, and stored as the ith element of the column vector $\underline{b}$. The result after iterating through all n rows of the matrix is an n by 1 column vector, $\underline{b}$. A^+ is then calculated and multiplied by $\underline{b}$, yielding the reconstructed fluorochrome concentration, $\underline{\hat{z}}$. A flowchart of this algorithm is shown in Figure 15, with acquired data shown in dark gray, calculated data in textured light gray, and methods in white.

Imaging Measurements

Generate Forward Model: W_{nB}, W_s and W_d

Normalized Born Field

Calculate and store:
$$\frac{D^{\lambda 2}}{v} W_{nB}^{-1} \underline{U}^{nB}$$

Multiply and store as b_i

Calculate row i of:
$$(W_s \odot W_d)^T$$

$i = i + 1$

Yes — Last row? — No

Multiply and store as $\underline{\hat{z}}$

Calculate and store A^+ matrix

Limiting step - memory

Reconstructed Fluorochrome Concentration

Figure 15. Row-Wise SVD-KR Reconstruction Algorithm

4.2.2. Method 2: Column-Wise SVD-KR Reconstruction

In this reconstruction method, one column at a time of the matrix $(W_s \odot W_d)^T$ is calculated and multiplied by the corresponding element of the vector $\frac{D^{\lambda 2}}{v} W_{nB}^{-1} \underline{U}^{nB}$. Iterating through all m columns of the matrix, the resulting vectors from each calculation

34

are summed resulting in the *n* by 1 column vector, $\underline{b}$. A^+ is then calculated and multiplied by $\underline{b}$, yielding the reconstructed fluorochrome concentration, $\underline{\hat{z}}$. A flowchart of this algorithm is shown in Figure 16, with acquired data shown in dark gray, calculated data in textured light gray, and methods in white.
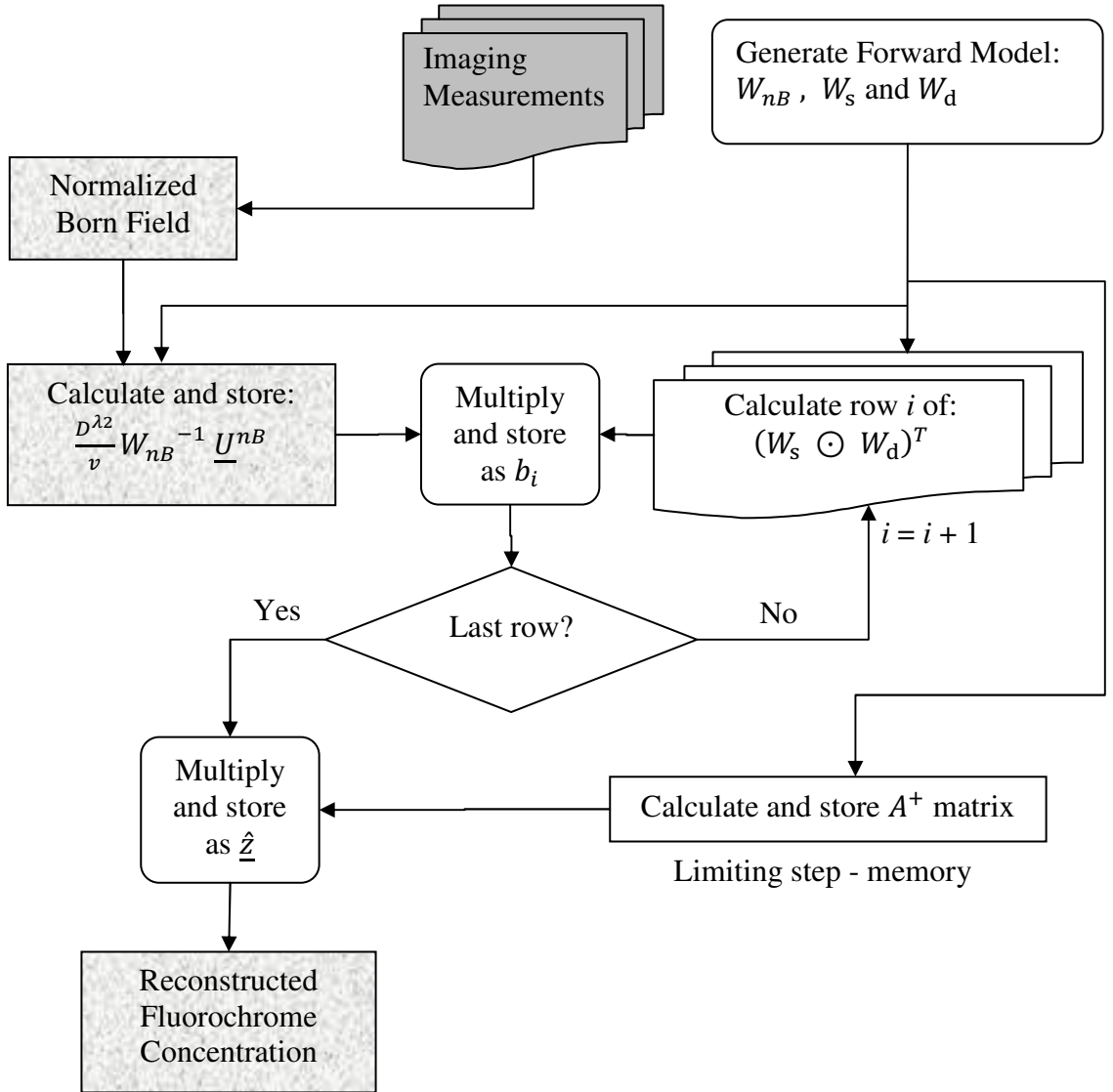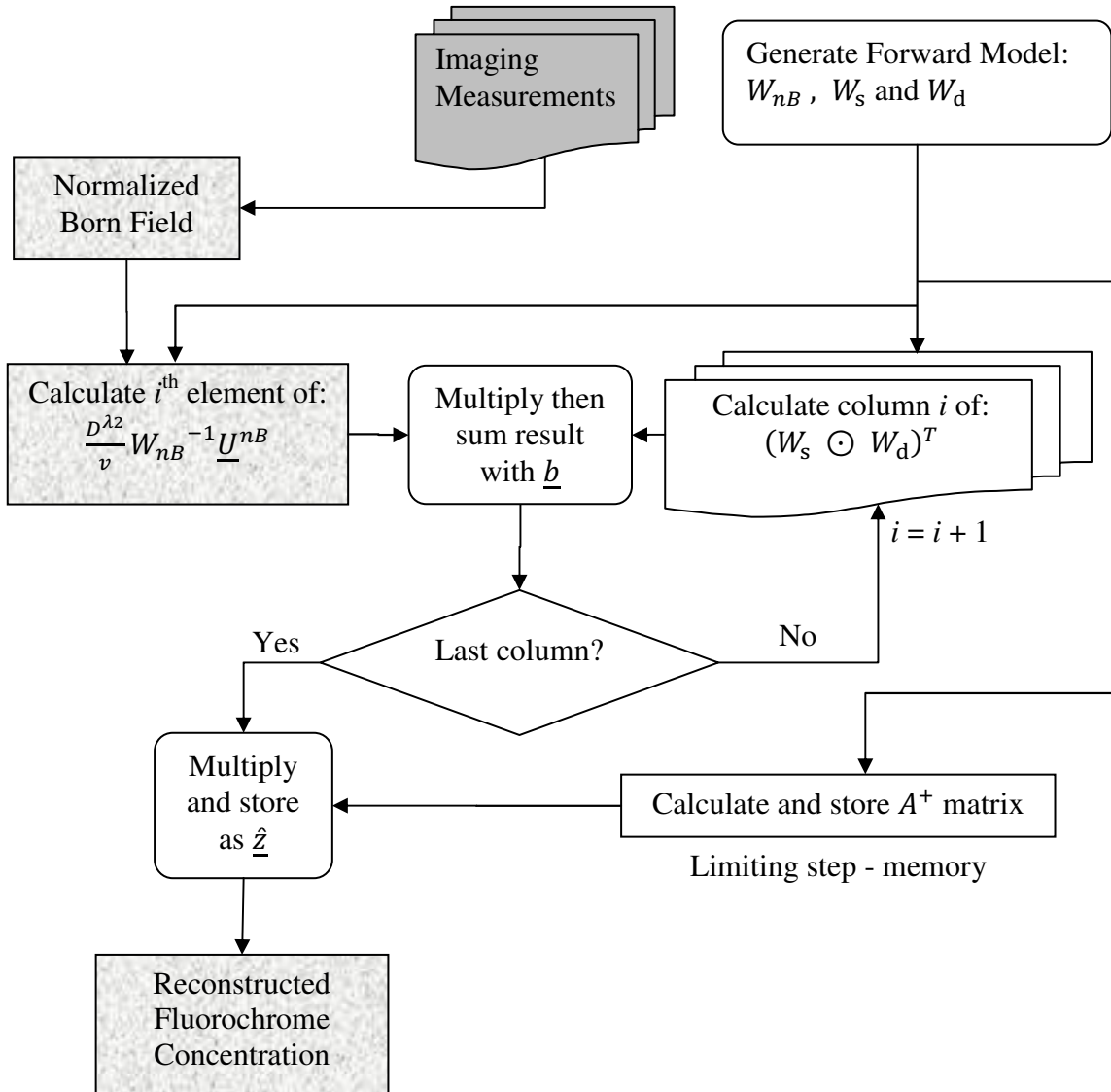

Figure 16. Column-Wise SVD-KR Reconstruction Algorithm

4.2.3. Minimizing Reconstruction Errors from Noisy Measurements

The reconstruction of FMT images is an ill-posed problem with a poorly conditioned weight matrix. Consequently, small errors in measurements or models can cause significant errors in the reconstruction. The least squares solution to the linear equation $A\underline{z} = \underline{b}$ is given by (60); the reconstruction error from this least squares solution is given by [14]

$$\frac{\|\delta\underline{z}\|}{\|\underline{z} + \delta\underline{z}\|} \leq \|A\|\|A^{-1}\| \times \frac{\|\delta A\|}{\|A\|} \tag{64}$$

$$\frac{\|\delta\underline{z}\|}{\|\underline{z} + \delta\underline{z}\|} \leq \|A\|\|A^{-1}\| \times \frac{\|\delta b\|}{\|b\|} \tag{65}$$

Combining (64) and (65) results in

$$\frac{\|\delta\underline{z}\|}{\|\underline{z} + \delta\underline{z}\|} \leq \|A\|\|A^{-1}\| \times \left[\frac{\|\delta\underline{b}\|}{\|\underline{b}\|} + \frac{\|\delta A\|}{\|A\|}\right] \tag{66}$$

where $\delta\underline{z}$ is the reconstruction error given by $\hat{\underline{z}} = \underline{z} + \delta\underline{z}$, $\delta\vec{b}$ is the measurement error, δA is the forward model error, and $\|A\|\|A^{-1}\|$ is the condition number of A. To better understand this equation and its implications, we need to first state the relationship between the singular value decomposition of A and the condition number of A. As shown in (42), A can be expressed as

$$A = U_A S_A V_A^{\ T} \tag{67}$$

where U_A and V_A are orthonormal matrices and S is a diagonal matrix of singular values arranged in a descending order. The norm of A, $\|A\|$, can then be written as

$$\|A\| = \|U_A\|\|S_A\|\|V_A^{\ T}\| \tag{68}$$

Since the norm of an orthonormal matrix is 1 and the norm of a diagonal matrix is equal

36

to the largest entry on the diagonal, $\|A\|$ is therefore equal to the largest singular value in S_A, σ_{max}. Likewise, $\|A^{-1}\|$ is equal to the inverse of the smallest singular value, σ_{min}^{-1}. Therefore the condition number of A is equal to

$$\|A\|\|A^{-1}\| = \frac{\sigma_{max}}{\sigma_{min}} \tag{69}$$

Inspecting (66), we can see that by reducing the condition number of A, the relative error in the reconstruction, $\|\delta\underline{z}\|/\|\underline{z} + \delta\underline{z}\|$, can be reduced as well. This can be accomplished by replacing A with a reduced rank approximation; assuming that A has n singular values, for $r < n$ a rank-r approximation to A, $\tilde{A}_r$, is equal to

$$\tilde{A}_r = U_{:r}S_r V_{:r}^T \tag{70}$$

where $U_{:r}$ is the first r columns of U_A, $V_{:r}$ is the first r columns of V_A, and S_r is diagonal matrix with the first r singular values of S_A. By using only the r largest singular values σ_{min} is increased, which decreases the condition number of $\tilde{A}_r$, leading to reduced reconstruction error. However, this approximation also introduces error by decreasing the accuracy of the forward model; the approximation error increases $\|\delta A\|/\|A\|$ in (66), leading to increased reconstruction error. Inspecting (66), we can see that for values of r that are not significantly less than n, $\|\delta\underline{b}\|/\|\underline{b}\| \gg \|\delta A\|/\|A\|$ and so the effect of increasing $\|\delta A\|/\|A\|$ will be less than the associated decrease of $\|A\|\|A^{-1}\|$. However, if r is decreased further, $\|\delta A\|/\|A\|$ can become a significant term when $\|\delta\underline{b}\|/\|\underline{b}\| \cong \|\delta A\|/\|A\|$, introducing a significant source of reconstruction error. Consequently, in selecting a value for r a balance must be struck, since lowering the value of r reduces the noise in the reconstruction but if lowered too far can introduce significant errors.

Previous research has addressed the issue of selecting r by analyzing the singular value decomposition of the weight matrix [15] [2]. As shown in (42), the singular value decomposition of the weight matrix is $W = USV^T$, which combined with (39) can be rewritten as [2]

$$U^T \underline{U}^{nB} = SV^T \underline{z} \tag{71}$$

$\underline{U}^{nB}$ can be decomposed into two components, $\underline{U}^{nB}_{signal}$ and $\underline{U}^{nB}_{noise}$, by analyzing multiple measurement sets [2]. The vectors $U^T \underline{U}^{nB}_{signal}$ and $U^T \underline{U}^{nB}_{noise}$ are calculated, filtered, and plotted; the value of r is selected as the index at which $U^T \underline{U}^{nB}_{signal}$ crosses and becomes smaller than $U^T \underline{U}^{nB}_{noise}$ [2]. At this index, addition of additional singular values to the approximation will contribute more noise to the reconstruction than signal, increasing the reconstruction error.

This method of selecting r can be extended for use in the reconstruction methods presented here. (67) and (60) can be combined and rewritten to obtain

$$U_A^T \underline{b} = S_A V_A^T \underline{z} \tag{72}$$

This equation can be combined with (63) to yield

$$\frac{D^{\lambda 2}}{v} \left[U_A^T (W_s \odot W_d)^T W_{nB}^{-1} \right] \underline{U}^{nB} = S_A V_A^T \underline{z} \tag{73}$$

Like before, $\underline{U}^{nB}$ can be decomposed into two components, $\underline{U}^{nB}_{signal}$ and $\underline{U}^{nB}_{noise}$, resulting in two equations,

$$\frac{D^{\lambda 2}}{v} \left[U_A^T (W_s \odot W_d)^T W_{nB}^{-1} \right] \underline{U}^{nB}_{signal} = S_A V_A^T \underline{z}_{signal} \tag{74}$$

$$\frac{D^{\lambda 2}}{v}\left[U_A{}^T \left(W_s \odot W_d\right)^T W_{nB}{}^{-1}\right] \underline{U}_{noise}^{nB} = S_A V_A{}^T \underline{z}_{noise} \tag{75}$$

The two resulting vectors from theses equations are filtered with a median filter and then plotted against each other. The highest index for which $S_A V_A{}^T \underline{z}_{signal} > S_A V_A{}^T \underline{z}_{noise}$ gives the value of r to use for the rank-r approximation of the matrix A. Figure 17 is an example for a reconstruction of 512 voxels using synthetic measurements from 256 sources and 1024 detectors with a 40 dB SNR. From the data used to generate Figure 17, the value of r was determined to be 262. To confirm this result, SVD-KR reconstructions were performed for $1 \le r \le 512$, and the RMS error measured against the known fluorochrome concentration. This analysis confirmed that $r = 262$ has the minimum root mean squared error (RMSE), with a value of 0.6370. A plot of the results is shown in Figure 18. It is worth noting that the value of r depends on many variables, such as measurement noise and the number and placement of voxels, sources and detectors. These plots were created using a synthetically generated FMT imaging data.
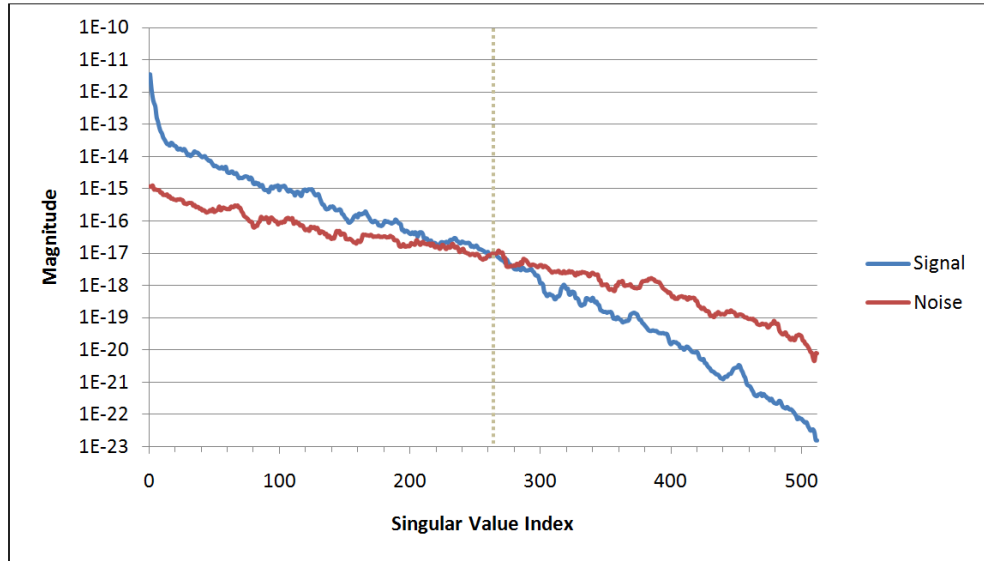

Figure 17. Plot of Signal and Noise Contributions vs. Singular Value Index
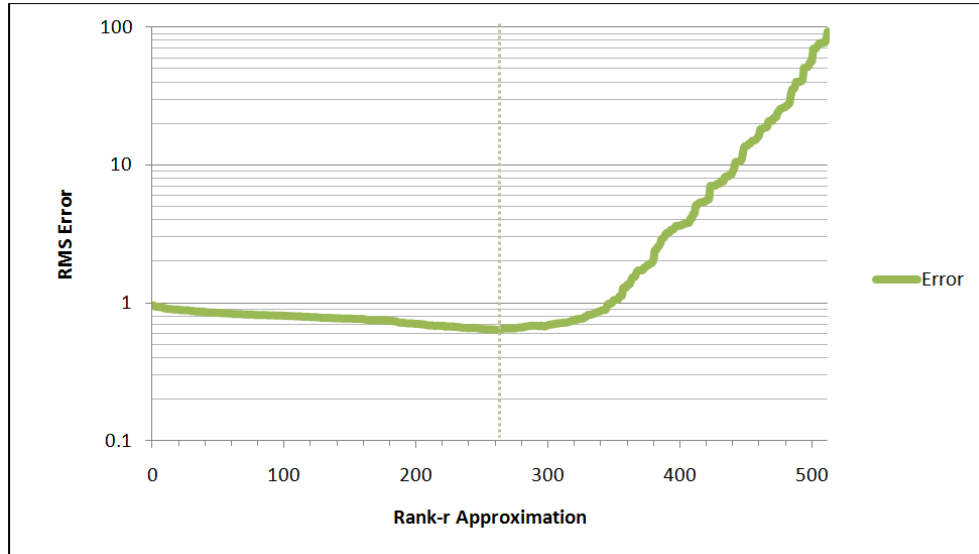
39

Figure 18. Reconstruction Error vs. Rank

4.3. Results for the New FMT Reconstruction

To solve (60) for $\hat{\underline{z}}$, the Moore-Penrose pseudoinverse of the matrix A must be calculated. The matrix A is of size n by n for any matrix W of size m by n, where n is the number of voxels in the forward model and m is the number of source-detector pairs. Since matrix A is of size n by n, the computational and memory complexity of calculating its pseudoinverse is dependent solely on the number of voxels in the forward problem and not on the number of source detector pairs; since this step is the limiting step in terms of memory usage, the reconstruction algorithm is able to solve for systems with a large number of sources and detectors.

Previous imaging systems have typically used an underdetermined system of equations for W because of the computational limitations of existing reconstruction techniques.

Compared to these existing techniques, the SVD-KR reconstruction method significantly reduces the computational complexity and memory requirements of reconstruction when the matrix W is overdetermined.

To test the performance of this method, synthetic volume image data was generated using a diffuse non-ellipsoidal phantom designed to emulate structures that may be encountered *in vivo*. A slice of this phantom is shown in Figure 19.

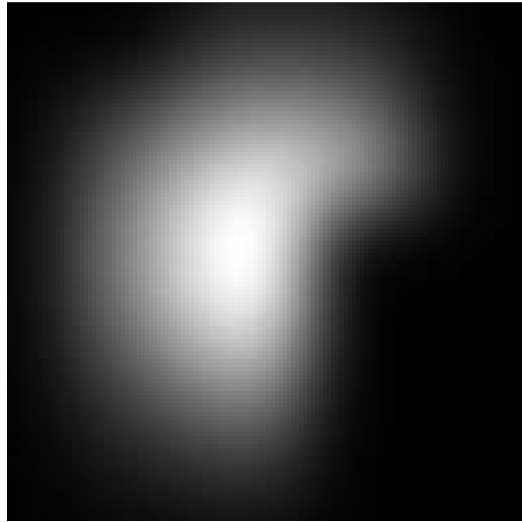Figure 19. Diffuse Non-ellipsoidal Phantom Used in Reconstruction

It was then reconstructed using three different reconstruction techniques: row-wise SVD-KR, column-wise SVD-KR, and singular value decomposition. For simplicity, these tests used an equal number of sources and detectors for each dataset. Results of this test are shown in Figure 20, Figure 21, Figure 22, Table 2, Table 3, Table 4, and Table 5.

Table 2. SVD-KR and SVD Reconstruction Time

Voxels	Source-Detector Pairs	Row-Wise SVD-KR Reconstruction Time (sec)	Column-Wise SVD-KR Reconstruction Time	SVD Reconstruction Time
1,000	10,000	4.7	4.7	11.4
1,000	50,625	6.4	7.2	31.4
1,000	160,000	14.2	13.8	86.1
1,000	390,625	29.7	28.3	709.6
1,000	810,000	62.2	52.9	Out of memory
1,000	2,560,000	211.0	165.2	Out of memory
1,000	6,250,000	454.4	378.3	Out of memory
1,000	12,960,000	1,022.6	803.2	Out of memory
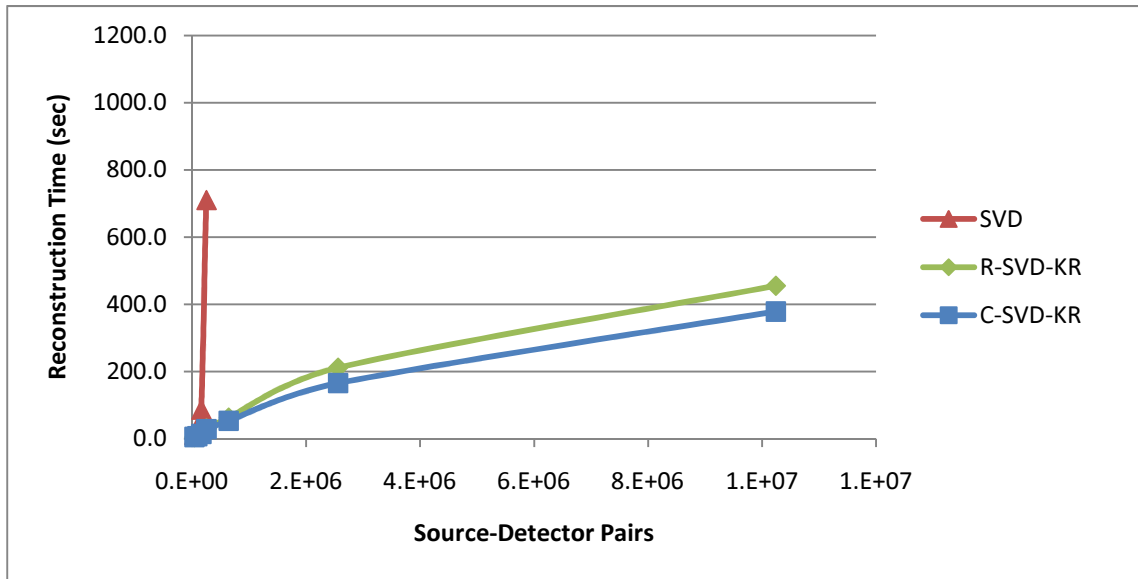
Figure 20. SVD-KR and SVD Reconstruction Time

Table 3. SVD-KR and SVD Calculated Reconstruction Memory Usage

Voxels	Source-Detector Pairs	Row-Wise SVD-KR Reconstruction Memory Usage (MB)	Column-Wise SVD-KR Reconstruction Memory Usage (MB)	SVD Reconstruction Memory Usage (MB)
1,000	10,000	37	37	305
1,000	50,625	44	44	1,545
1,000	160,000	55	55	4,883
1,000	390,625	69	69	11,921
1,000	810,000	85	85	24,719
1,000	2,560,000	128	128	78,125
1,000	6,250,000	183	183	190,735
1,000	12,960,000	250	250	395,508

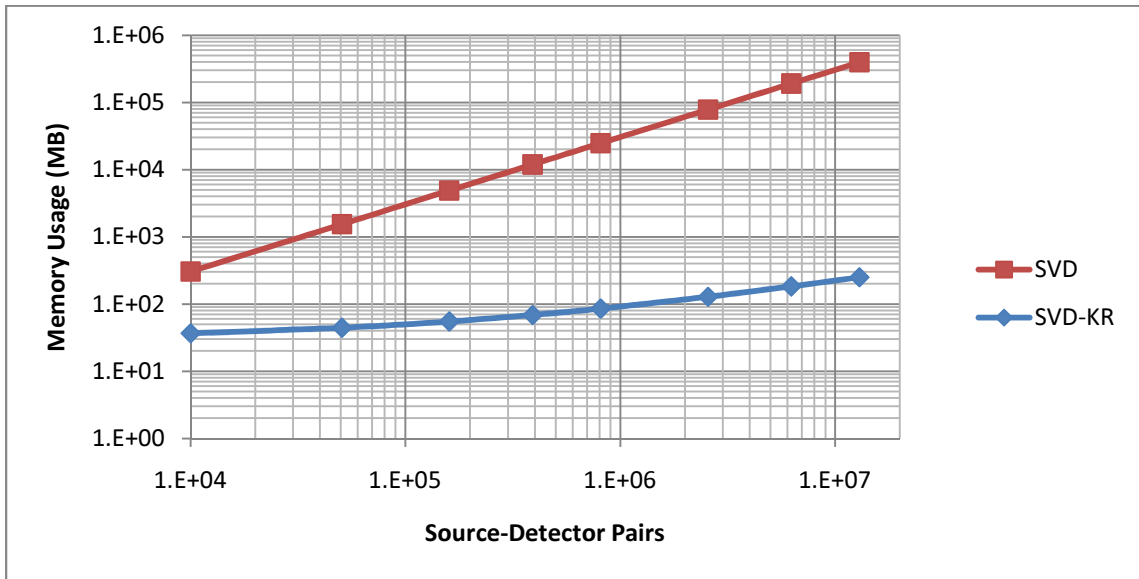Figure 21. SVD-KR and SVD Calculated Reconstruction Memory Usage

43

Table 4. SVD-KR and SVD Reconstruction Errors

Voxels	Source-Detector Pairs	Row-Wise SVD-KR Reconstruction RMSE	Column-Wise SVD-KR Reconstruction RMSE	SVD Reconstruction RMSE
1,000	10,000	0.472	0.472	0.423
1,000	50,625	0.402	0.402	0.339
1,000	160,000	0.332	0.332	0.293
1,000	390,625	0.301	0.301	0.283
1,000	810,000	0.272	0.272	Out of memory
1,000	2,560,000	0.243	0.243	Out of memory
1,000	6,250,000	0.234	0.234	Out of memory
1,000	12,960,000	0.220	0.220	Out of memory
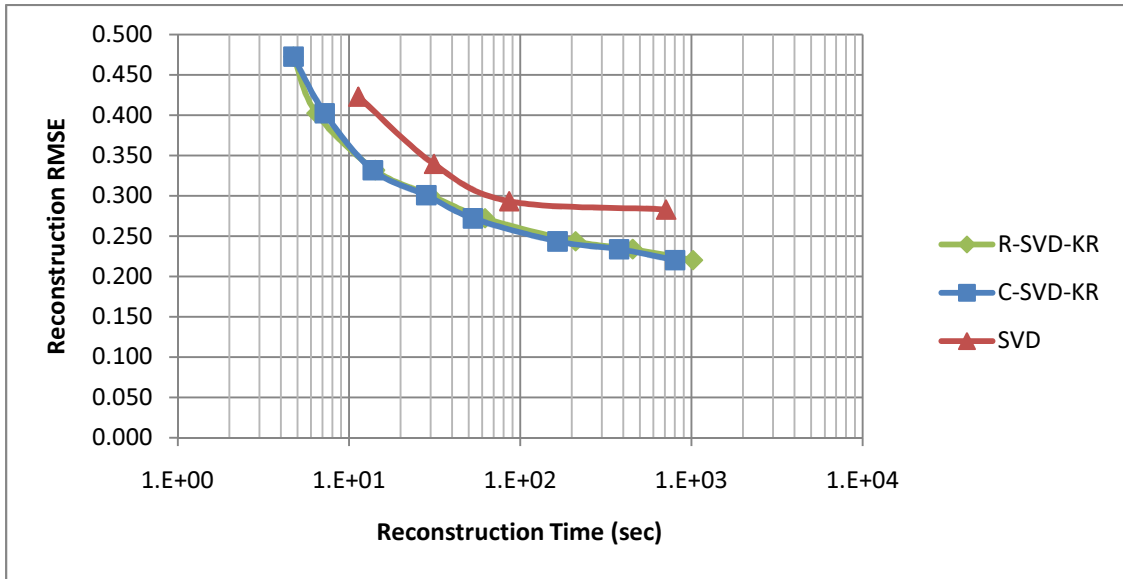
Figure 22. Reconstruction Time vs. RMSE

From these results, we can see that the SVD-KR reconstructions were significantly faster than SVD reconstruction, with speed increases of up to 25X. The column-wise SVD-KR reconstruction method performed slightly faster than the row-wise SVD-KR. SVD-KR was able to reconstruct four large datasets that could not be reconstructed by the SVD reconstruction algorithm; the largest dataset would have needed approximately 386 GB

44

of memory for reconstruction with SVD. Error was slightly higher for the SVD-KR reconstructions compared to the SVD reconstructions when solving for the same measurement dataset. However, Figure 22 shows that SVD-KR can reconstruct to the same accuracy as SVD in less time. Alternatively, SVD-KR can reconstruct more accurately than SVD in the same time.

Since the previous datasets used an equal number of sources and detectors, new datasets were generated to determine the effect of the source to detector ratio on reconstruction. The results are shown in Table 5.

Table 5. SVD-KR Reconstruction Time and Error

Voxels	Source-Detector Pairs	Sources	Detectors	Row-Wise SVD-KR Reconstruction		Column-Wise SVD-KR Reconstruction	
				Time	Error	Time	Error
1000	640000	6400	100	45.4	0.541	37.1	0.541
1000	640000	1600	400	47.7	0.441	41.8	0.441
1000	640000	400	1600	48.0	0.493	44.0	0.493
1000	640000	100	6400	53.0	0.523	38.2	0.523

These results show that reconstruction error is minimized when the ratio between sources and detectors is near one. Many current FMT setups use more detectors than sources; in order to make best use of SVD-KR reconstruction, the number of sources in new systems needs to be increased. Additionally, since measurement sets from large detector arrays can be reconstructed using this method, many additional CCD cameras could be arrayed around the sample to collect additional measurements. The improved detector spatial diversity and spatial sampling in such a system would reduce error in the reconstruction.

As an example of the image reconstructions obtained using SVD-KR, a 24 x 24 x 24 voxel image was reconstructed using imaging data from 9216 sources and 9216 detectors with a signal to noise ratio of 40 dB. The results are shown in Figure 23.
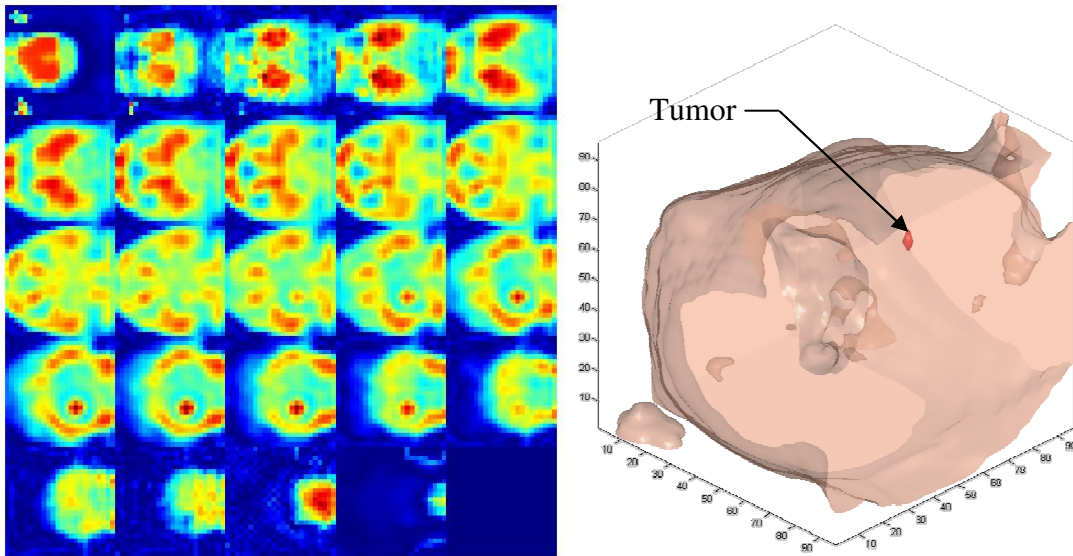

Figure 23. Reconstruction Using SVD-KR. Montage on left, 3-D rendering on right.

5. Modeling of Photon Diffusion

The reconstruction of FMT images is an ill-posed problem, with a poorly conditioned weight matrix; consequently, small errors in the forward model can create significantly larger errors in the reconstructed image. Improving the prediction accuracy of the photon propagation forward model would therefore allow for significant increases in the accuracy and image quality of FMT reconstructions. In this chapter, we will study photon diffusion in media with homogeneous and heterogeneous optical properties.

A finite element model is developed in COMSOL, and is validated using existing models. COMSOL is a finite element based multi-physics simulation program. Finite element models discretize the volume into a set of nodes and elements. This allows a continuous function to be approximated. Additionally, the finite element mesh is able to adapt the size of elements where necessary in order to better approximate the function near boundaries and small features such as point sources. This finite element model is then used to study the effects of heterogeneous optical properties on the accuracy of the normalized Born field in models that assume homogeneous optical properties.

5.1. Photon Propagation Model for Homogeneous Media

Photon diffusion in homogeneous media was modeled using two different approaches: finite element modeling in COMSOL, and method of sources using Green's function.

5.1.1. Finite Element Model

The diffusion approximation to the radiative transfer equation, given by (1), was modeled for a 3-D imaging system using COMSOL 3.4a. The photon density inside of the imaging chamber, $U(\vec{r}, t)$, was solved for using stationary analysis of the partial differential equation given by (1). A schematic of the imaging chamber setup is shown in Figure 24.
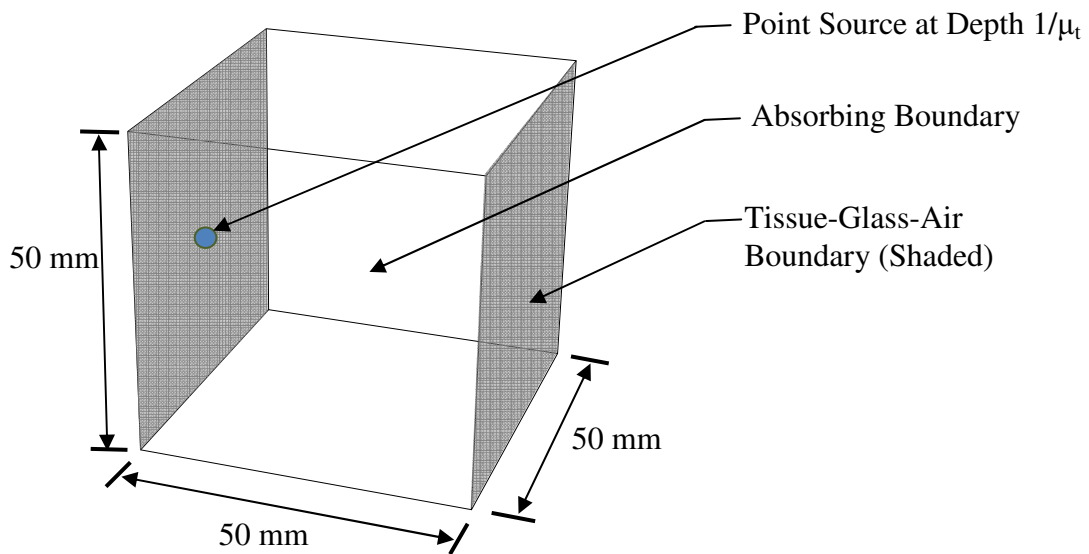

Figure 24. Imaging Chamber Schematic for COMSOL Simulation

The imaging chamber was modeled as a $50 \times 50 \times 50 \ mm^3$ cube. Two different boundary conditions were applied to the chamber; Absorbing boundaries were modeled with the Dirichlet condition from (8), while tissue-glass-air interfaces located at the source plane and detector plane were modeled with the modified Robin condition from (9) though (15). The glass was assumed to be treated with an anti-reflective coating, giving a value of $q = 0.5$ for the modified Robin conditions. The incident collimated

laser light was modeled as an isotropic point source at depth $z_0 = [\mu_s + (1 - g)\mu_s]^{-1}$ [4]. Optical properties inside the imaging chamber were assumed homogeneous with $n = 1.4$, $\mu_a = 0.03/\text{mm}$ and $\mu_s' = 1.0/\text{mm}$.

5.1.2. Method of Sources with Green's Function

To validate the precision of the above COMSOL finite element model, a model was constructed based on the method of sources [16] and Green's function [5] given by (34). Like the COMSOL model above, the incident collimated light is modeled as an isotropic point source at a depth of z_0 [4]. Zero photon density boundary conditions were assumed at absorbing boundaries and at an extrapolated boundary offset z_b from glass-tissue-air interfaces [16],

$$z_b = 2D \frac{1 + R_{eff}}{1 - R_{eff}} \tag{76}$$

where D is the diffusion coefficient, and R_{eff} is the Fresnel reflection at the boundary. For anti-reflection coating glass, it was assumed that $R_{eff} = 0$. These boundary conditions were met by adding additional positive and negative isotropic point sources [16]. Figure 25 shows how these boundary conditions were enforced the at the source.
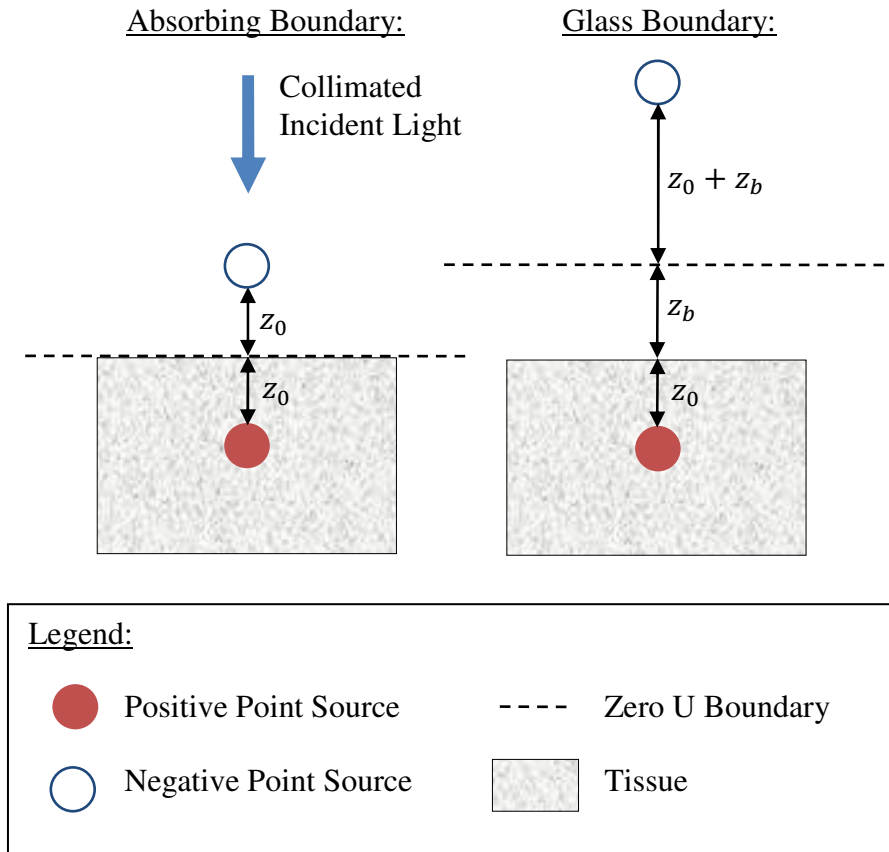
Figure 25. Source Boundary Conditions

In general, to enforce a boundary condition a copy of the point source(s) with opposite sign needs to be mirrored across the boundary. Multiple boundary conditions can be enforced by mirroring the point sources across each boundary. Figure 26 shows how this would be accomplished for the 4 boundary conditions from the 4 sides of a square imaging system.

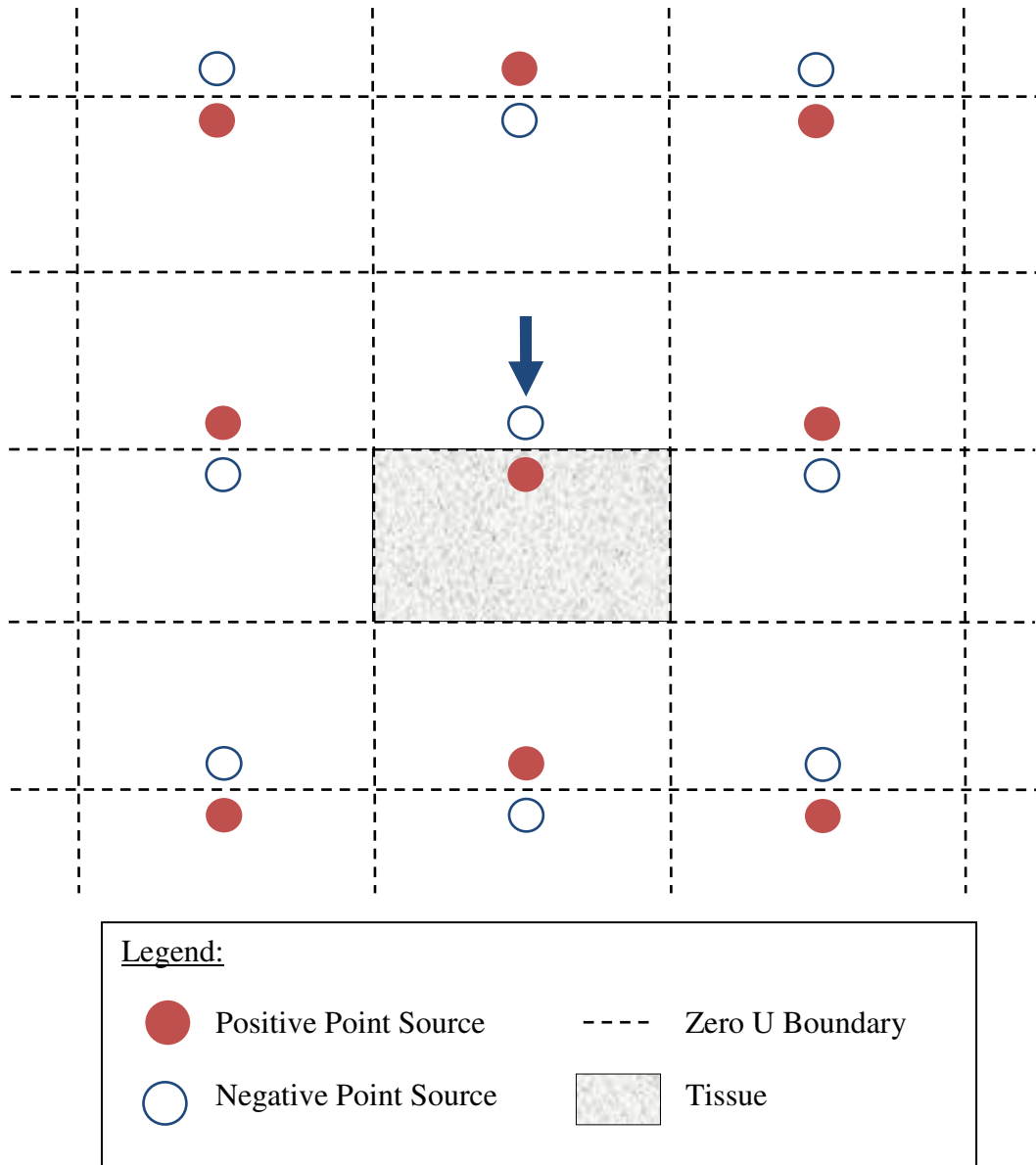Figure 26. 2-D Method of Sources to Enforce Boundary Conditions

Although hard to visualize, the method of sources presented in Figure 26 can be extended

to 3-D to enforce the 6 boundary conditions from the 6 sides of the cubic imaging

chamber. For the 3-D case, Figure 26 can be thought of as a perpendicular slice though

the imaging chamber that contains the source. While 4 of the 6 sides of the imaging

chamber intersect the page, 2 sides of the imaging chamber would lie parallel to the page, above and below; to enforce these 2 boundary conditions, all of the sources in Figure 26 would need to be mirrored over each of these boundaries - into and out of the page respectively.

5.1.3. Model Comparison

A 3-D method of sources model with 36 sources was constructed in MATLAB. The photon density in the imaging chamber induced by each source is given by (34). To compensate for differences in Θ_s between the two models, a MATLAB symbolic equation was built with the form:

$$f = \sum_{all\ sources} \pm\, a\, \frac{exp\,(jkx)}{4\pi vDx} \tag{77}$$

where $k = [(v\mu_a + j\omega)/D]^{1/2}$, $D = [3(1-g)\mu_s]^{-1}$, x is the distance from the source, and a is a symbolic variable to allow for the determination of an optimum value of Θ_s to compensate for differences in source intensity between the two models. The resulting equation was fit to the COMSOL data using MATLAB surface fitting tool, this is shown in Figure 27. Referring to Figure 25(a), for a 1-D system with 2 sources (77) becomes

$$f = \frac{a}{4\pi vD}\left[\frac{exp\,(jk(z-z_0))}{(z-z_0)} - \frac{exp\,(jk(z+z_0))}{(z+z_0)}\right] \tag{78}$$

Recall that v is the speed of light in the media, D is given by (4), $z_0 = [\mu_s + (1-g)\mu_s]^{-1}$, and $k = [(v\mu_a + j\omega)/D]^{1/2}$.
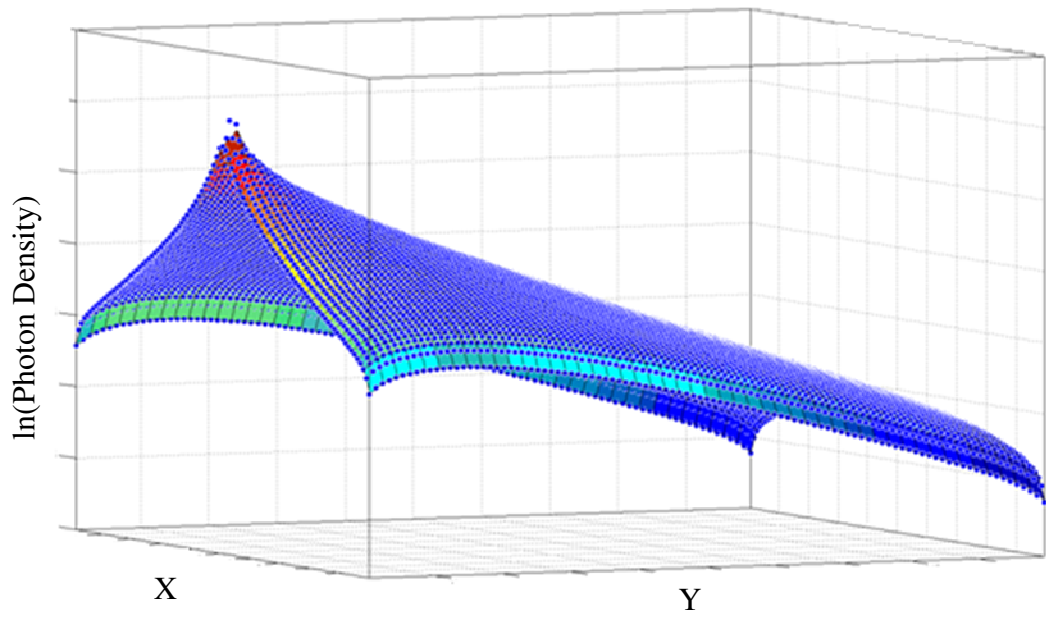
52

Figure 27. Surface Fit of Finite Element Model by Method of Sources Model
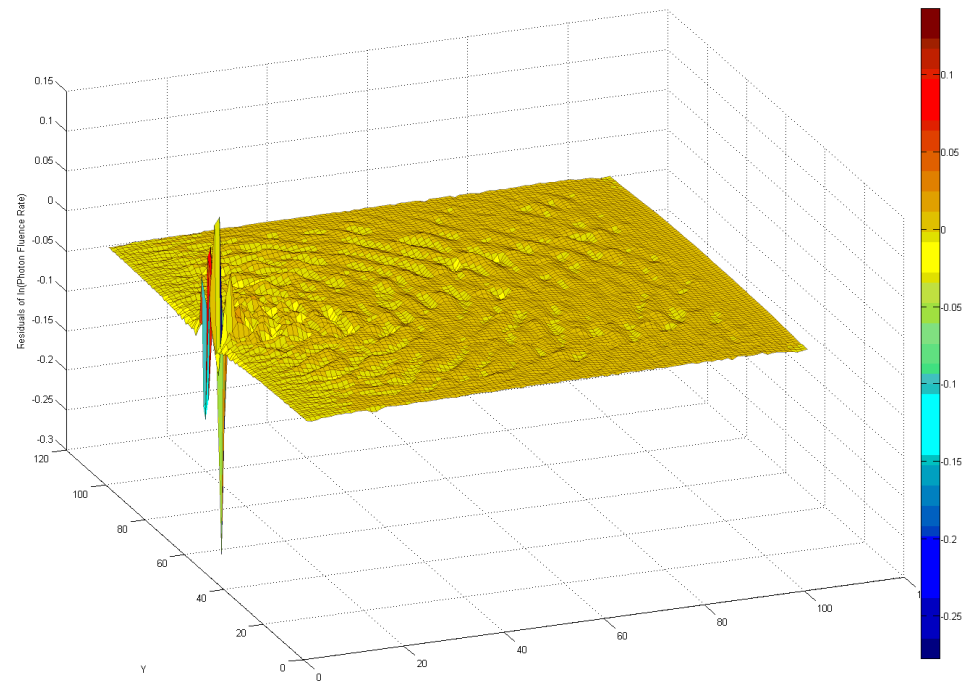

Figure 28. Residuals of Surface Fit

53

A value of $a = 1.003$ was found to minimize error between the two models, resulting in a RMSE of 0.004991. Further than 1 mm from the source, the models had a maximum error of 8%. Much of this error was likely the result of interpolating values from a finite element mesh used in COMSOL into a regular grid.

5.2. Finite Element Model for Heterogeneous Media

Many previous FMT imaging systems have used forward models which do not explicitly take into account the heterogeneous optical properties of the various tissues being imaged [1] [2] [5] [17]. Instead, it is assumed that the optical properties in the tissue are homogenous and equal to the average optical properties of the tissues; errors introduced by heterogeneous optical properties are partially canceled out by dividing fluorescent measurements by intrinsic measurements to obtain the normalized Born field. This provides an accurate approximation when small, simple heterogeneities are present, such as those found in deliberately constructed phantoms. However, to resolve deep structures with high resolution *in vivo* despite the complex anatomical structures and the diverse optical properties of tissue, a forward model that more accurately takes into account heterogeneous optical properties is necessary.

One promising forward model involves using a hybrid CT-FMT system; In such a system, anatomical data would be collected by the CT system concurrently with fluorescent data by the FMT system. The CT dataset could be used to determine the shape of anatomical structures, classify their composition, and then lookup their known optical properties. The shape and composition of the anatomical structures extracted from

54

the CT data could then be used to accurately model photon propagation using finite element methods. The photon density data generated by this method could then be used in a reconstruction method such as the SVD-KR reconstruction method presented in the previous chapter.

5.2.1. CT Image Segmentation

From the images produced by the CT scanner, anatomical structures can be extracted by one of many image segmentation techniques [18]. For the purposes of this paper, k-means clustering based image segmentation was used, however other image segmentation techniques would be suitable as well. Image segmentation was performed on the Digimouse CT dataset [19] [20].

The right hind leg of the mouse was cropped from the dataset and segmented using k-means clustering based on the voxel intensity. Based on the major structures present in the leg, the voxel intensities were grouped into 5 clusters: bone, skin/fat, fast twitch muscle, slow twitch muscle, and the surrounding air. Initial values were set manually using typical values for these structures. The voxel intensity values for the 5 clusters were obtained using a k-means clustering algorithm; these values were used to segment the dataset into the tissue types represented by the clusters based on the intensity of each voxel. Each tissue was then converted into a 3-D mesh. The resulting 3-D structures are shown in Figure 30.
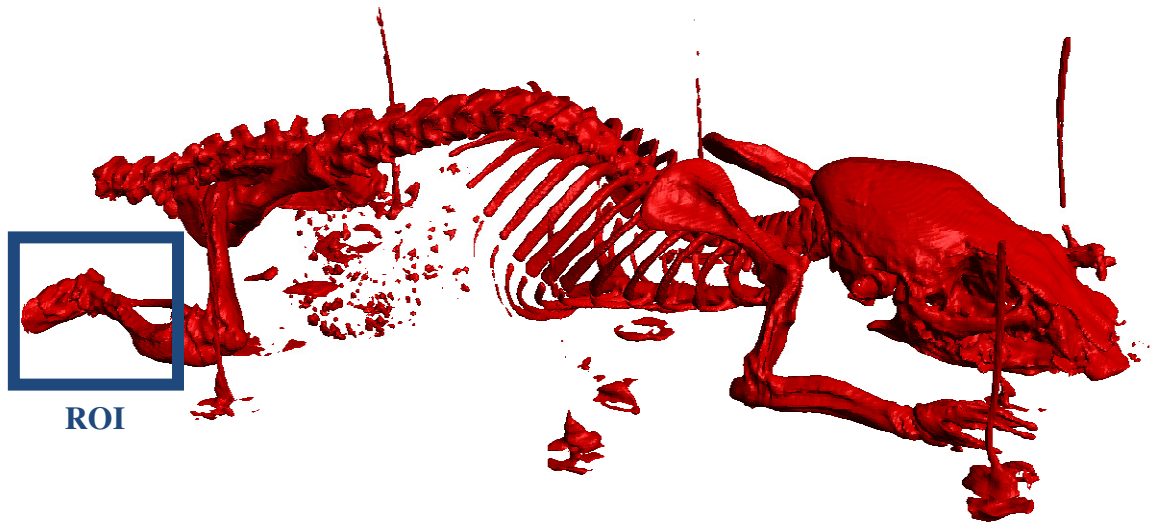
Figure 29. Segmented Digimouse Skeleton Showing Region of Interest (ROI)

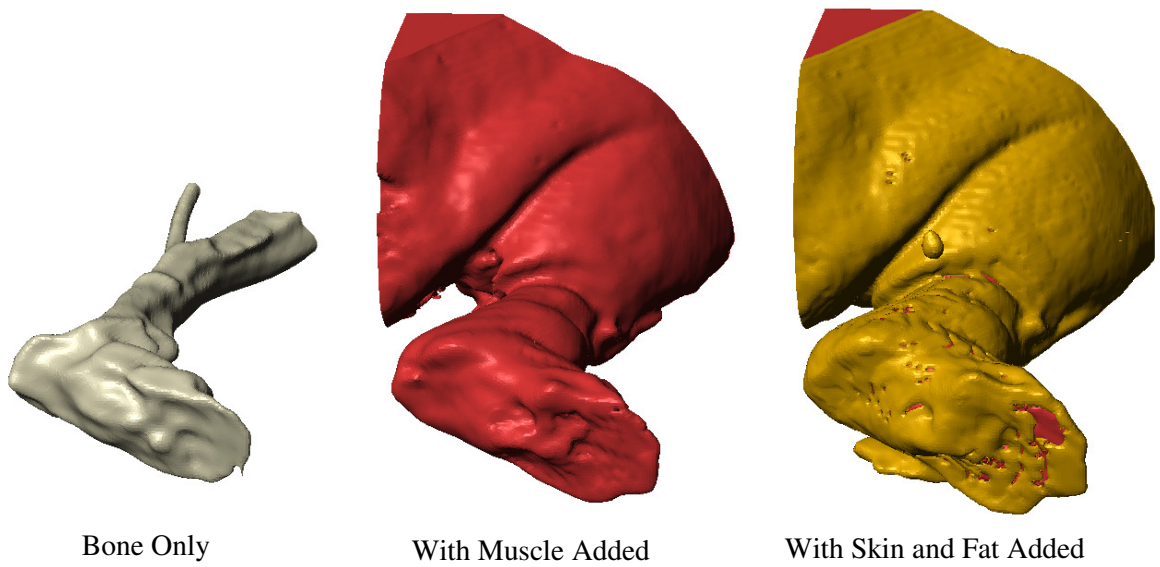Bone Only   With Muscle Added   With Skin and Fat Added

Figure 30. Segmented Mouse Leg

5.2.2. Finite Element Modeling of Photon Propagation

To analyze photon propagation through heterogeneous media, the 3-D meshes shown in Figure 30 were imported into COMSOL. The photon density inside of the imaging

chamber, $U(\vec{r}, t)$, was solved using stationary analysis of the following partial differential equation:

$$\frac{\partial}{\partial t} U(\vec{r}, t) - \nabla \cdot [vD(\vec{r}) \nabla U(\vec{r}, t)] + v\mu_a(\vec{r}) U(\vec{r}, t) = S(\vec{r}, t) \qquad (79)$$

This is a more general form of (1) which is valid for heterogeneous optical properties. A schematic of the imaging chamber setup is shown in Figure 31.
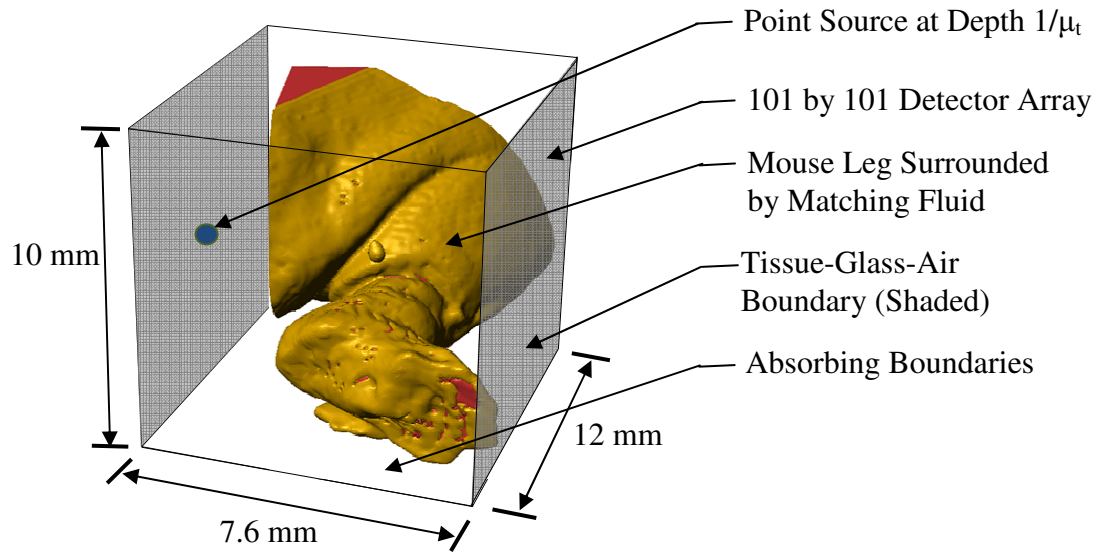

Figure 31. Imaging Chamber Schematic for Heterogeneous COMSOL Simulation

A small amount of fluorochrome, modeled as a point source, was placed between the fat and muscle on the lateral face of the right lower leg. The optical properties for each of the tissues were assigned the following values:

Table 6. Optical Properties of Selected Tissue

Tissue	Source	μ_a	$(1-g)\mu_s$	μ_s	g	D
		mm^{-1}	mm^{-1}	mm^{-1}	-	mm
Bone	Pig Skull [7]	0.04	2.625	35	0.925	0.125
Muscle	Chicken [3]	0.017	0.33	0.41	0.20	0.961
Skin	Murine Dermis (Albino) [3]	0.28	6.2	23.9	0.74	0.051
Matching Fluid	Intralipid and Ink Solution [2]	0.03	1.0	0.1	0.90	0.324

By building a similar model with the correct physical layout of the sources, detectors and imaging chamber, this model can be used to calculate the W_{nB}, W_s, and W_d matrices from (53) for many FMT imaging systems. This method offers the advantage of explicitly taking into account heterogeneous optical properties, leading to increased model accuracy and more accurate reconstructions.

5.3. Precession of Normalized Born Field in Heterogeneous Media

The model from chapter 5.2.2 was used to generate two sets of synthetic measurement data, differing only in the optical properties of the mouse leg; one with the heterogeneous optical properties listed in Table 6, the other with homogeneous optical properties equal to the matching fluid. Fluorescent and intrinsic measurements were taken with each system for one source by a 101 by 101 array of detectors.

The normalized Born field was calculated for each measurement set, and the error calculated. The root mean squared error (RMSE) was found to be 0.2985. While the accuracy of these heterogeneous and homogeneous measurements cannot be determined

without experimental measurements, the low precession in the normalized Born field measurements between two measurement sets that differ only in the assumption of homogeneity shows that the normalized Born field can have errors of at least this magnitude introduced by this assumption. However, the normalized Born field did significantly reduce the errors introduced by heterogeneous optical properties compared to non-normalized measurements, which were found to have an RMSE over 50 times larger.

To validate the accuracy of the above homogeneous measurement set, a third measurement set was synthetically generated using homogeneous optical properties and the method of sources from chapter 5.1.2. The error between the normalized Born fields of the two homogeneous measurement sets was found to be 0.0180.

6. Administering and Imaging Multiple Fluorochromes Simultaneously

There are a variety of commercially available fluorochromes that vary in biological target, excitation wavelength and fluorescent wavelength. Different classes of fluorochromes include antibody conjugate probes, nucleic acid probes, cell function probes and fluorescent proteins. The ability to image multiple distinct probes simultaneously, and independently reconstruct the distribution of each probe could increase the visibility of low contrast targets, and allow researchers to better understand relationships between biological processes.

Existing FMT reconstruction techniques can be extended to reconstruct the distribution of multiple fluorochromes. A mixture of two or more fluorochromes with affinities for different biological targets would be injected into the subject by a single syringe, and be distributed by blood flow and diffusion until interacting with their respective targets. These fluorochromes would be chosen to emit light of different wavelength when excited by a single excitation wavelength. Figure 32 shows a synthetic example of intensity vs. wavelength for an imaging system with a source of light with peak wavelength λ_1, and two fluorochromes that fluoresce with peak wavelengths λ_2 and λ_3.
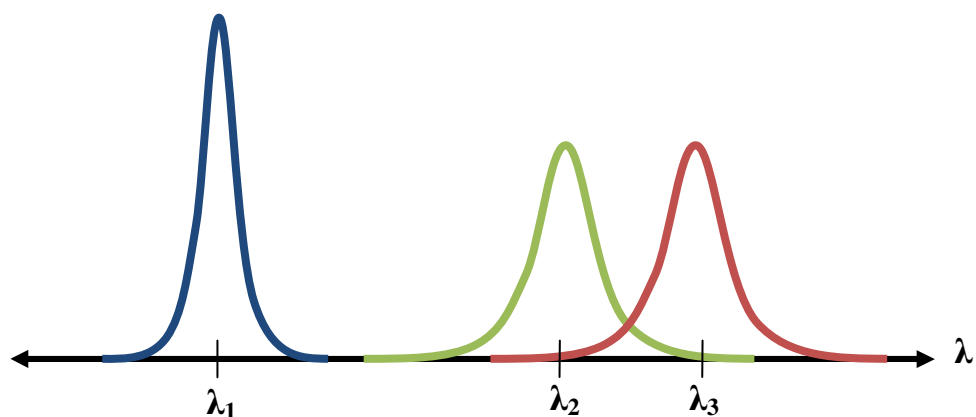
Figure 32. Synthetic Intensity vs. Wavelength Measured at Detector

Transmission measurements in a typical single fluorochrome system are taken with one CCD camera fitted with a band-pass filter. Transmission measurements in a multi-fluorochrome system would still be taken by one CCD camera, however this camera would have a changeable band-pass filter for each distinct fluorochrome. Images would be acquired using the same procedures for acquiring single fluorochrome FMT images [2]. For each source, three separate images would be acquired by a CCD camera with a different filter used for each image; One band-pass filter for each peak frequency, λ_1, λ_2, and λ_3. Alternatively, three CCD cameras could be used, each with a different filter, resulting in faster acquisition times but potentially introducing errors due to their different physical positions. Either of the above methods would result in three sets of measurements: one for the intrinsic illumination at the excitation wavelength, λ_1, and one for each fluorochrome, λ_2 and λ_3. These measurements are collected into a matrix, one column for each wavelength,

$$U(\vec{r}_{sd}, :) = \begin{bmatrix} U_{\lambda_1}(\vec{r}_{sd}) & U_{\lambda_2}(\vec{r}_{sd}) & U_{\lambda_3}(\vec{r}_{sd}) \end{bmatrix} \tag{80}$$

This matrix, U, is of size m by 3 where m is equal to the number of source-detector pairs. Since band-pass filters for each peak wavelength do not exclude all of the light from the source or other fluorochromes, this matrix is a mixture of the columns of a more fundamental matrix, U^B, that describes the true photon intensity at the detector from the source and each of the fluorochromes. The matrix U^B can be calculated by multiplying U by the Moore-Penrose pseudoinverse of the mixing matrix, R, where R is given by

$$R = \begin{bmatrix} \Theta_{11} & \Theta_{12} & \Theta_{13} \\ \Theta_{21} & \Theta_{22} & \Theta_{23} \\ \Theta_{31} & \Theta_{32} & \Theta_{33} \end{bmatrix} \tag{81}$$

where Θ_{ij} is the coefficient that corrects for the transmittance of λ_i thru the filter for λ_j. It could have appropriately been called $\Theta_{\lambda_i, \lambda_j}$, however this simpler notation is being used for convenience. If no filter is used for λ_1 [2], the matrix R can be simplified to

$$R = \begin{bmatrix} 1 & \Theta_{12} & \Theta_{13} \\ 1 & \Theta_{22} & \Theta_{23} \\ 1 & \Theta_{32} & \Theta_{33} \end{bmatrix} \tag{82}$$

Multiplying U by the Moore-Penrose pseudoinverse of the matrix R results in the unmixed Born field for each fluorescent wavelength, U^B,

$$U^B = U \times R^+ \tag{83}$$

This expression can be expanded to

$$\begin{bmatrix} U^B_{:\lambda_1} & U^B_{:\lambda_2} & U^B_{:\lambda_3} \end{bmatrix} = \begin{bmatrix} U_{:\lambda_1} & U_{:\lambda_2} & U_{:\lambda_3} \end{bmatrix} \times \begin{bmatrix} R^+_{11} & R^+_{12} & R^+_{13} \\ R^+_{21} & R^+_{22} & R^+_{23} \\ R^+_{31} & R^+_{32} & R^+_{33} \end{bmatrix} \tag{84}$$

where R^+_{ij} is the element of R^+ in the ith row and j^{th} column, $U^B_{:\lambda_i}$ is the ith column of U^B,

and $U_{:\lambda_i}$ is the ith column of U. The matrix U^B can be normalized to obtain an approximation to the normalized Born field by performing an element-wise division of the first column of U^B into the other columns of U^B,

$$U^{nB}(\vec{r}_{sd}, :) = \begin{bmatrix} \dfrac{U_{:\lambda_2}^B(\vec{r}_{sd})}{U_{:\lambda_1}^B(\vec{r}_{sd})} & \dfrac{U_{:\lambda_3}^B(\vec{r}_{sd})}{U_{:\lambda_1}^B(\vec{r}_{sd})} \end{bmatrix} \tag{85}$$

The matrix U^{nB} is of size m by 2 where m is equal to the number of source-detector pairs. This matrix can then be used to solve for the concentration of fluorochrome using many standard methods of FMT reconstruction, including the method of projections, singular value decomposition, and SVD-KR. More generally, the solution can be written as

$$\hat{z} = W^{-1} U^{nB} \tag{86}$$

The resulting matrix $\hat{z}$ will be of size n by 2, where n is equal to the number of voxels in the forward problem. Each column of $\hat{z}$, $\hat{z}_i$, is a vector representing the concentration of the fluorochrome with fluorescent wavelength λ_{i+1}.

6.1. Results

A phantom was created from the Digimouse dataset, and two different types of fluorochromes were synthetically injected. To test the ability of imaging multiple fluorochromes to enhance the image quality for low contrast targets, the fluorochromes were assumed to have a concentration 4 times greater in their target than the surrounding tissue. The low contrast makes identification of the target difficult in the reconstructed image; however, when two or more fluorochromes are imaged simultaneously, the background can be canceled out to increase the contrast of the target.

A measurement dataset with signal mixing was generated using the phantom. The dataset was reconstructed using row-wise SVD-KR reconstruction. The results for a slice of the reconstruction that contains both targets is shown in Figure 33. The results indicate that imaging using multiple fluorochromes can allow for enhanced detection of low contrast targets.
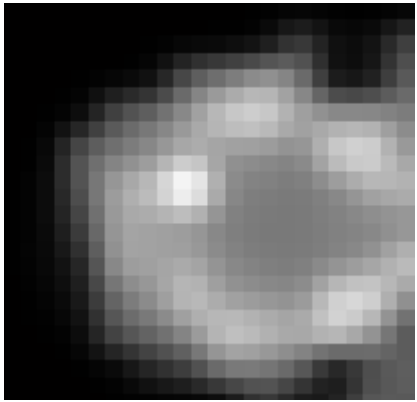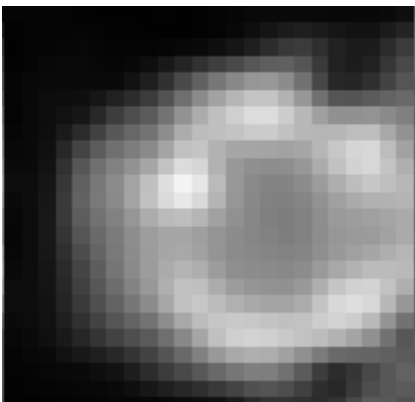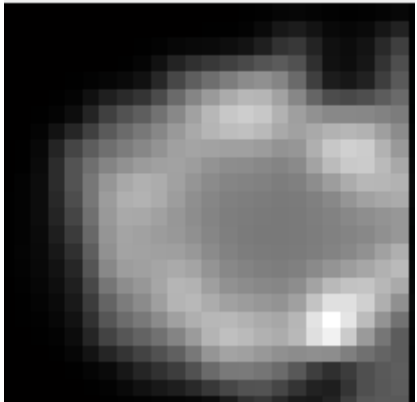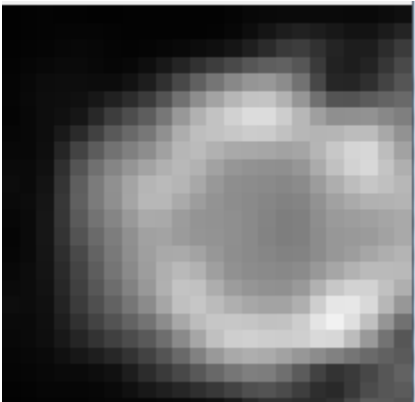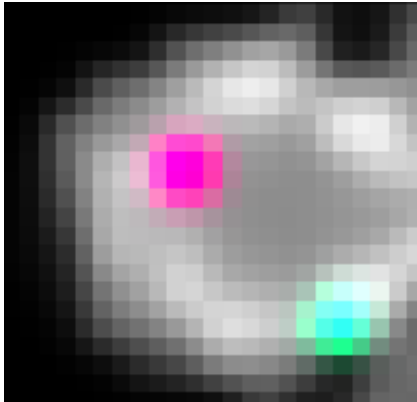
	Original	Reconstruction
Fluorochrome 1		
Fluorochrome 2		
Fluorochrome 1 and 2 Combined - Variations Colored		

Figure 33. Multi-fluorochrome Imaging with Contrast Enhancement

7. Parallel Processing Implementations

Parallel computing allows for multiple processors to simultaneously carry out calculations. This allows for increased reconstruction speed and for reconstructions of large numbers of voxels using large imaging datasets. Parallel reconstruction algorithms have the potential to increase reconstruction resolution, reconstruction image quality and imaging volume.

7.1. Parallel Reconstruction by SVD-KR

SVD-KR reconstruction can be implemented in parallel environments, allowing for decreased reconstruction times. To evaluate the performance of SVD-KR algorithms in a parallel environment, reconstructions were performed with different numbers of processor cores in a shared memory environment. The results of these reconstructions are shown in Table 7 and Figure 34 below. These results show that both row-wise SVD-KR and column-wise SVD-KR see performance gains in a parallel environment. However, because of communication overhead and a serial SVD algorithm, the gains are not proportional to the number of processor cores used. If implemented using a parallel SVD algorithm, larger speed increases would be expected.

Table 7. SVD-KR Parallel Reconstruction Time and Relative Speed

Voxels	Source-Detector Pairs	Sources	Detectors	Processor Cores	Row-Wise SVD-KR Reconstruction		Column-Wise SVD-KR Reconstruction	
					Time	Speed-up	Time	Speed-up
1728	331776	576	576	1	66.6	100%	52.9	100%
1728	331776	576	576	2	51.4	129%	39.2	135%
1728	331776	576	576	3	48.0	139%	35.2	150%
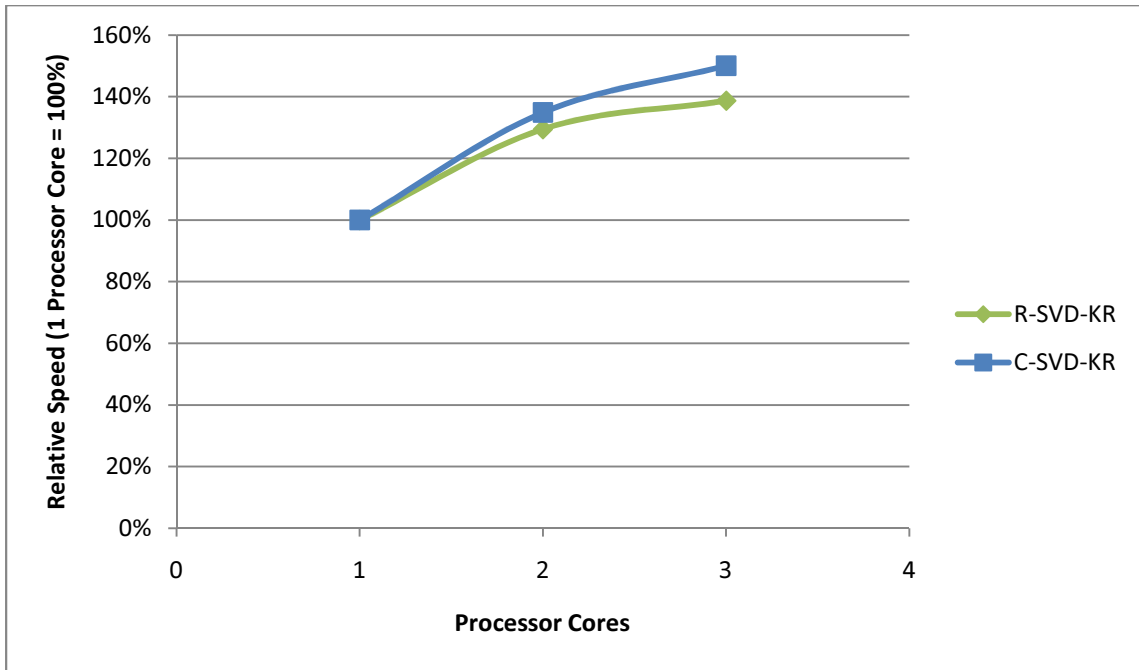
Figure 34. SVD-KR Parallel Reconstruction Relative Speed

7.2. Two-Stage Approach for Larger Imaging Volumes

A two-stage approach could be utilized to reconstruct larger imaging volumes. In this approach, the imaging volume is initially reconstructed with low resolution, and the resolution of a selected region is subsequently enhanced by a second reconstruction. A simple 2-D example of region of interest enhancement is shown in Figure 35.
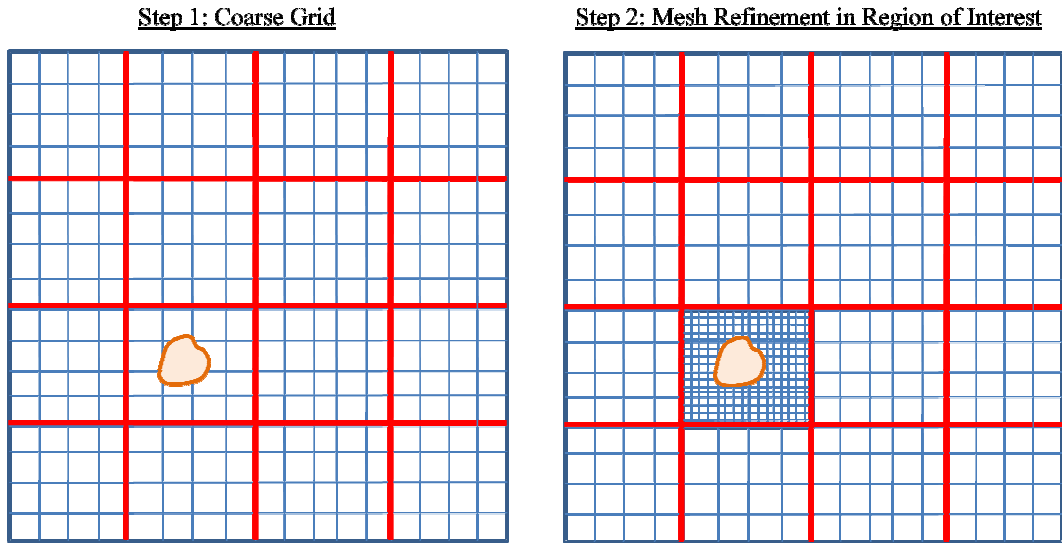
Figure 35. Mesh Refinement in Region of Interest

This algorithm could be parallelized by having each computer independently refine a different region of the imaging chamber. Once all of the regions in the imaging chamber where enhanced, they could be combined into a single high resolution image.

Attempts made to create a working algorithm ran into problems. Increasing the resolution in the region of interest created a twofold problem: the condition number of the weight matrix significantly increased, while the low resolution reconstruction of other regions increased the model error. With the increase in both condition number and model error, reconstruction errors increased significantly leading to an overall decrease in image quality. This algorithm is presented here for the interest of the reader, with the hope that it will allow someone to improve upon it in the future.

7.2.1. Implementing SVD Region of Interest Enhancement

To enhance the resolution in the region of interest, the matrix W will need to be updated; consequently, the SVD of W will need to be updated for reconstruction. Calculating the singular value decomposition of the matrix W as shown in (30) can be intensive in both computational and memory requirements for the large, overdetermined matrices needed for a high resolution FMT reconstruction. Since the SVD of the matrix W is already known from the initial low resolution reconstruction, the SVD of W can be updated directly, as opposed to updating W and recalculating its SVD; this can significantly reduce the computational and memory complexity of reconstruction when W is overdetermined.

7.2.2. SVD Column Removal Update

Refining the reconstruction resolution in a small region of interest requires the modification of the matrix W after initially calculating the singular value decomposition. To remove the original voxels in this region from the forward model, columns of data need to be removed from the matrix W and the singular value decomposition of this new matrix W' is calculated. Instead of recalculating the singular value decomposition of the matrix W' from the entire matrix W', the known singular value decomposition of W can be updated with the newly appended data, significantly reducing the computational complexity. This method will work for removal of any set of arbitrary columns, however to simplify the formalism without loss of generality a set of sequential columns will be removed in this example. Given a matrix W of size m by n, for which the rank-r singular value decomposition is known,

$$W = USV^T \qquad (87)$$

If an array of columns D of size m by Δn is removed from W,

$$W = [W_1' \quad D \quad W_2'] \qquad (88)$$

$$W' = [W_1' \quad W_2'] \qquad (89)$$

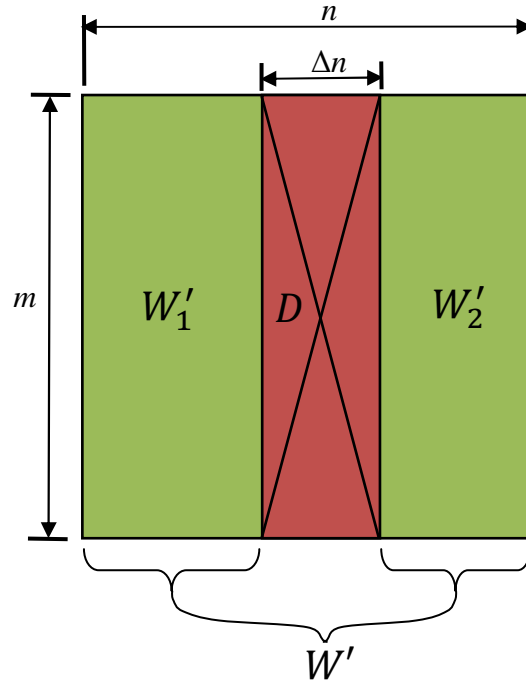Figure 36. Removing Columns from the Weight Matrix

The known singular value decomposition of W can be updated to obtain the singular value decomposition of matrix W',

$$W' = U'S'V'^T \qquad (90)$$

First, remove the columns of V^T that correspond to the columns of D, these columns are at the same indexes in the matrix V^T as the matrix W.

$$V^T = [V_1^T \quad V_D^T \quad V_2^T] \qquad (91)$$

$$V_{W'}^T = [V_1^T \ V_2^T] \tag{92}$$

This operation causes a loss of orthogonality in the matrix $V_{W'}^T$. To restore orthogonality, the matrix $V_{W'}^T$ can be decomposed into an orthogonal and an upper triangular matrix by the QR decomposition,

$$Q, R \overset{QR}{\leftarrow} V_{W'}^T \tag{93}$$

where Q is an orthogonal basis of $V_{W'}^T$, and R is an upper triangular matrix. W' can then be rewritten as

$$W' = USV'^T = US(QR)^T = USR^TQ^T = UAQ^T \tag{94}$$

Where $A = SR^T$. U and Q^T are both orthogonal matrices however, A is not diagonal. To make A diagonal, its singular value decomposition is calculated,

$$A = U_A S_A V_A^T \tag{95}$$

W' can then be written as

$$W' = U(U_A S_A V_A^T)Q^T = (UU_A)S_A(QV_A)^T \tag{96}$$

The final formulation for W' is therefore

$$W' = U'S'V'^T \tag{97}$$

where

$$U' = UU_A \tag{98}$$

$$S' = S_A \tag{99}$$

$$V' = QV_A \tag{100}$$

This method is to the best of my knowledge a new result. The advantages of this method is that it allows the singular value decomposition of W' to be determined to a high degree of accuracy by calculating the singular value decomposition of A. Since the size of A can

be significantly smaller than *W'*, this method can significantly decrease the computational and memory complexity of updating the singular value decomposition of a matrix when columns of data are removed.

7.2.3. SVD Column Addition Update

Refining the reconstruction resolution in a small region of interest requires the modification of the matrix *W* after initially calculating the singular value decomposition. To incorporate the new voxels in this region into the forward model, columns of data need to be appended to the matrix *W* and the singular value decomposition of this new matrix *W'* is calculated. Instead of recalculating the singular value decomposition of the matrix *W'* from the entire matrix *W'*, the known singular value decomposition of *W* can be updated with the newly appended data, significantly reducing the computational and memory complexity. Given a matrix *W* of size *m* by *n*, for which the rank-r singular value decomposition is known,

$$W = USV^T \tag{101}$$

If an array of new columns C of size *m* by Δn is appended to *W*,

$$W' = [W \ \ C] \tag{102}$$
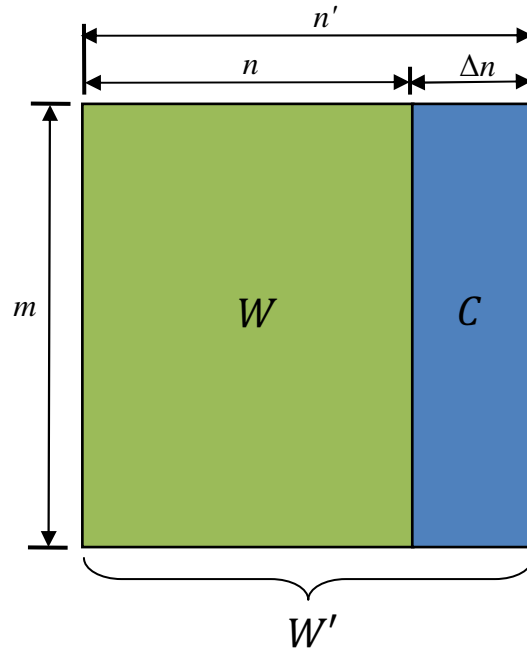
Figure 37. Appending Columns to the Weight Matrix

the known singular value decomposition of W can be updated to obtain the singular value

decomposition of matrix W',

$$W' = U'S'V'^T \tag{103}$$

First, let [21]

$$L = U^T C \tag{104}$$

$$H = (I - UU^T)C = C - UL \tag{105}$$

L is then the projection of C onto the orthonormal basis U, and H is the component of C

orthogonal to U. Next, find the QR decomposition of H [21],

$$J, K \xleftarrow{QR} H \tag{106}$$

where J is an orthogonal matrix, and K is an upper triangular matrix. W' is equal to [21]

$$W' = [W \ C] = [U \ J]\begin{bmatrix} S & L \\ 0 & K \end{bmatrix}\begin{bmatrix} V & 0 \\ 0 & I \end{bmatrix}^T \tag{107}$$

Upon inspection, the left and right matrices in the matrix product are orthogonal, however the middle matrix, denoted Q, is not diagonal. To make Q diagonal requires finding its singular value decomposition [21],

$$U_Q, S_Q, V_Q \xleftarrow{SVD} Q \ \text{ where } \ Q = \begin{bmatrix} S & L \\ 0 & K \end{bmatrix} \tag{108}$$

The updated singular value decomposition is therefore [21]

$$W' = U'S'V'^T \tag{109}$$

where [21]

$$U' = [U \ J]U_Q \tag{110}$$

$$S' = S_Q \tag{111}$$

$$V' = \begin{bmatrix} V & 0 \\ 0 & I \end{bmatrix}V_Q \tag{112}$$

This procedure takes $O\big((m+n)r^2 + m(\Delta n)^2\big)$ time, most of which is for the matrix multiplications that rotate the subspace shown in (101), (102) and (103) [21].

8. Conclusions

Since SVD-KR reconstruction significantly reduces the computational complexity and memory requirements for reconstruction of overdetermined imaging datasets, imaging systems with larger detector arrays, higher spatial sampling, and a larger number of sources can be reconstructed; this improves the information content of the measurements and decreases the ill-posedness of the inverse problem, leading to increased resolution and accuracy for *in vivo* FMT imaging [2]. Compared to reconstruction with SVD, the SVD-KR reconstruction method decreased reconstruction time up to 25 times and decreased memory usage by up to three orders of magnitude. Consequently, SVD-KR reconstruction allows for fast, high resolution reconstructions with low reconstruction error. To make best use of this new reconstruction method, FMT imaging systems would be designed to have a large number of sources and detectors. Future research will be necessary to design a FMT imaging system that takes advantage of SVD-KR for reconstructions of large detector arrays with a large number of sources.

The SVD-KR reconstruction method can be used for a variety of forward models. In one compatible model, CT imaging data from a combined CT/FMT system could be segmented into separate tissues; the known optical properties these tissues along with their 3-D shape could allow for more accurate approximations to the photon density *in vivo*. Paired with improvements in the accuracy of the forward model, SVD-KR could

allow for FMT reconstructions of sufficient resolution and quality to be clinically meaningful, and significantly expand the applications of FMT.

9. List of References

[1] R. B. Schulz, J. Ripoll, and V. Ntziachristos, "Experimental Fluorescence Tomography of Tissues With Noncontact Measurements," *IEEE Transactions on Medical Imaging*, vol. 23, no. 4, pp. 492-500, 2004.

[2] E.E. Graves, J. Ripoll, R. Weissleder, and V. Ntziachristos, "A submillimeter resolution fluorescence molecular imaging system for small animal imaging," *Medical Physics*, vol. 30, no. 5, pp. 901-911, 2003.

[3] W. F. Cheong, S. A. Prahl, and A. J. Welsh, "A Review of the Optical Properties of Biological Tissues," *IEEE Journal of Quantum Electronics*, pp. 2166-2185, 1990.

[4] M. S. Patterson, B. Chance, and B. C. Wilson, "Time resolved reflectance and transmittance for the noninvasive measurement of tissue optical properties," *Applied Optics*, vol. 28, no. 12, pp. 2331-2336, 1989.

[5] V. Ntziachristos and R. Weissleder, "Experimental three-dimensional fluorescence reconstruction of diffuse media by use of a normalized Born approximation," *Optics Letters*, vol. 26, no. 12, pp. 893-895, 2001.

[6] J. P. Culver et al., "Three-dimensional diffuse optical tomography in the parallel plane transmission geometry: Evaluation of a hybrid frequency domain continuous wave clinical system for breast imaging," *Medical Physics*, vol. 30, no. 2, pp. 235-247, 2003.

[7] M. Firbank, M. Hiraoka, M. Essenpreis, and D. T. Delpy, "Measurement of the optical properties of the skull in the wavelength range 650-950 nm," *Phys. Med. Biol.*, vol. 38, pp. 503-510, 1993.

[8] T.C. Zhu and J. Lee, "Finite-element modeling of light fluence distribution in prostate during photodynamic therapy," in *Excerpt from the Proceedings of the COMSOL Multiphysics User's Conference*, Boston, 2005.

[9] M. Schwieiger, S. R. Arridge, M. Hiraoka, and D. T. Delpy, "The finite element method for the propagation of light in scattering media: Boundary and source conditions," *Med. Phys.*, vol. 22, no. 11, pp. 1779-1792, 1995.

[10] J.B. Fishkin and E. Gratton, "Propagation of photon-density waves in strongly scattering media containing an absorbing semi-infinite plane bounded by a straight edge," *J. Opt. Soc. Am. A.*, vol. 10, no. 1, pp. 127-140, 1993.

[11] A. C. Kak and M. Slaney, *Principles of Computerized Tomographic Imaging*. New York: IEEE Press, 1988.

[12] J. P. Culver, V. Ntziachristos, M. J. Holboke, and A. G. Yodh, "Optimizationzation of optode arrangements for diffuse optical tomography: A singular value analysis," *Opt. Lett.*, vol. 26, pp. 701-703, 2001.

[13] T. Kolda, "Multilinear operators for higher-order decompositions," Sandia National Laboratories, Albuquerque, New Mexico, 2006.

[14] A. K. Kaw, *Introduction to Matrix Algebra*, Second Edition ed. Tampa, 2008.

[15] J. P. Culver, V. Ntziachristos, M. J. Holboke, and A. G. Yodh, "Optimization of optode arrangements for diffuse optical tomography: A singular value analysis," *Opt. Lett.*, vol. 26, pp. 701-703, 2001.

[16] R. C. Haskell et al., "Boundary conditions for the diffusion equation in radiative transfer," *J. Opt. Soc. Am. A*, vol. 11, no. 10, pp. 2727-2741, Oct. 1994.

[17] A. Sourbret, J. Ripoll, and V. Ntziachristos, "Accuracy of Fluorescent Tomography in the Presence of Heterogeneities: Study of the Normalized Born Ratio," *IEEE Transactions on Medical Imaging*, vol. 24, no. 10, pp. 1377-1389, 2005.

[18] D. L. Pham, C. Xu, and J. L. Prince, "Current Methods in Medical Image Segmentation," *Annual Review of Biomedical Engineering*, vol. 2, pp. 315-337 , August 200.

[19] B. Dogdas, D. Stout, A. Chatziioannou, and R. M. Leahy, "Digimouse: A 3D Whole Body Mouse Atlas from CT and Cryosection Data," *Phys Med Biol.*, vol. 52, no. 3, pp. 577-87, Feb 2007.

[20] D. Stout et al., "Creating a whole body digital mouse atlas with PET, CT and cryosection images.," *Molecular Imaging and Biology*, vol. 4, no. 4, p. S27, 2002.

[21] M. Brand, "Incremental Singular Value Decomposition Of Uncertain Data With Missing Values," in *In ECCV*, 2002, pp. 707-720.

[22] B. C. Wilson and S. L. Jacques, "Optical Reflectance and Transmittance of Tissues: Principles and Applications," *IEEE Journal of Quantum Electronics*, vol. 26, no. 12, pp. 2186-2197, 1990.

[23] W. Cong, K. Durairaj, L. V. Wang, and G. Wang, "A Born-type approximation method for bioluminescence tomography," *Medical Physics*, vol. 33, no. 3, p. 679, 2006.

About the Author

Stephen J. Shamp was born in Akron, OH and earned a B.S. degree in electrical engineering from the University of Notre Dame. He is currently a candidate for a M.S. degree in electrical engineering at the University of South Florida. After graduating, he is going to pursue a M.S. degree in Physiology at the University of Cincinnati, with hopes of continuing thereafter to medical school.